Tomographic Imaging of the Fermi-LAT γ-Ray Sky through Cross-correlations: A Wider and Deeper Look

Cuoco, A.; Bilicki, M.A.; Xia, J.; Branchini, E.

Tomographic Imaging of the *Fermi*-LAT γ-Ray Sky through Cross-correlations: A Wider and Deeper Look

Alessandro Cuoco[2], Maciej Bilicki[3,4,5] , Jun-Qing Xia[1] , and Enzo Branchini[6,7,8]

[1] Department of Astronomy, Beijing Normal University, Beijing 100875, P. R. China; xiajq@bnu.edu.cn
[2] Institute for Theoretical Particle Physics and Cosmology, RWTH Aachen University, Otto-Blumenthal-Strasse, D-52057, Aachen, Germany; cuoco@physik.rwth-aachen.de
[3] Leiden Observatory, Leiden University, P.O. Box 9513, NL-2300 RA Leiden, The Netherlands; bilicki@strw.leidenuniv.nl
[4] National Center for Nuclear Research, Astrophysics Division, P.O. Box 447, 90-950 Łódź, Poland
[5] Janusz Gil Institute of Astronomy, University of Zielona Góra, ul. Lubuska 2, 65-265 Zielona Góra, Poland
[6] Dipartimento di Matematica e Fisica, Università degli Studi "Roma Tre", via della Vasca Navale 84, I-00146 Roma, Italy
[7] INFN, Sezione di Roma Tre, via della Vasca Navale 84, I-00146 Roma, Italy
[8] INAF Osservatorio Astronomico di Roma, INAF, Osservatorio Astronomico di Roma, Monte Porzio Catone, Italy; branchin@fis.uniroma3.it
Received 2017 May 19; revised 2017 July 24; accepted 2017 August 7; published 2017 September 1

Abstract

We investigate the nature of the extragalactic unresolved γ-ray background (UGRB) by cross-correlating several galaxy catalogs with sky maps of the UGRB built from 78 months of Pass 8 *Fermi*-Large Area Telescope data. This study updates and improves similar previous analyses in several aspects. First, the use of a larger γ-ray data set allows us to investigate the energy dependence of the cross-correlation in more detail, using up to eight energy bins over a wide energy range of [0.25,500] GeV. Second, we consider larger and deeper catalogs (2MASS Photometric Redshift catalog, 2MPZ; *WISE* × SuperCOSMOS, WI×SC; and SDSS DR12 photometric redshift data set) in addition to the ones employed in the previous studies (NVSS and SDSS QSOs). Third, we exploit the redshift information available for the above catalogs to divide them into redshift bins and perform the cross-correlation separately in each of them. Our results confirm, with higher statistical significance, the detection of cross-correlation signals between the UGRB maps and *all* the catalogs considered, on angular scales smaller than 1°. Significances range from 16.3σ for NVSS, 7σ for SDSS DR12 and WI×SC, to 5σ for 2MPZ and 4σ for SDSS QSOs. Furthermore, including redshift tomography, the significance of the SDSS DR12 signal strikingly rises up to $\sim12\sigma$ and that of WI×SC to $\sim10.6\sigma$. We offer a simple interpretation of the signal in the framework of the halo model. The precise redshift and energy information allows us to clearly detect a change over redshift in the spectral and clustering behavior of the γ-ray sources contributing to the UGRB.

Key words: cosmology: observations – cosmology: theory – gamma rays: diffuse background – large-scale structure of universe

1. Introduction

The extragalactic γ-ray background (EGB) is the gamma-ray emission observed at high galactic latitudes after subtraction of the diffuse emission from our Galaxy. It is mainly contributed by various classes of astrophysical sources, like common star-forming galaxies (SFGs) and active galactic nuclei (AGNs) such as blazars. Contributions from purely diffuse processes, for example cascades from ultra-high-energy cosmic rays, are also possible, as well as exotic scenarios like γ-rays from dark matter (DM) annihilation or decay (see Fornasa & Sanchez-Conde 2015 for a review). In the era of the *Fermi* Large Area Telescope (LAT; Atwood et al. 2009), with its strong sensitivity to point sources, a sizable fraction of the EGB has been resolved into sources. Indeed, the third *Fermi* γ-ray catalog of sources (3FGL; Acero et al. 2015) contains ~3000 sources. The resolved sources constitute typically 10%–20% of the EGB for energies below ~10 GeV, while above this energy the fraction rises up to 50% or more (Ackermann et al. 2015, 2016). This large number of detected sources has been fundamental to studying in detail the different populations of emitters and inferring their properties in the so-far unresolved regime (Ackermann et al. 2011, 2012a; Inoue 2011; Ajello et al. 2012, 2014; Di Mauro et al. 2014a, 2014c). The still-unresolved EGB emission is typically given the name of unresolved (or isotropic) gamma-ray background (UGRB;

Ackermann et al. 2015) and is the subject of the present analysis.

Together with population studies of resolved sources, in recent years a number of different and complementary techniques have been developed to study the UGRB in a more direct way, exploiting the information contained in the spatial and the energy properties of the UGRB maps. Among these we can list anisotropy analyses (Ando & Komatsu 2006, 2013; Ando 2009; Ackermann et al. 2012c; Cuoco et al. 2012; Harding & Abazajian 2012; Fornasa et al. 2013, 2016; Di Mauro et al. 2014b; Ando et al. 2017), pixel statistic analyses (Dodelson et al. 2009; Malyshev & Hogg 2011; Feyereisen et al. 2015; Lisanti et al. 2016; Zechlin et al. 2016a, 2016b), and cross-correlations with tracers of the large-scale structure of the universe (Ando 2014; Ando et al. 2014; Fornengo & Regis 2014; Shirasaki et al. 2014; Camera et al. 2015; Cuoco et al. 2015; Fornengo et al. 2015; Regis et al. 2015; Xia et al. 2015; Feng et al. 2017; Shirasaki et al. 2016; Tröster et al. 2017), which we will investigate in the following.

In Xia et al. (2015; hereafter X15), Cuoco et al. (2015), and Regis et al. (2015), gamma-ray maps of the UGRB from five years of *Fermi*-LAT data were cross-correlated with different catalogs of galaxies, namely SDSS DR6 quasars (Richards et al. 2009), SDSS DR8 Luminous Red Galaxies (Abdalla et al. 2011), NVSS radio galaxies (Condon et al. 1998), 2MASS galaxies (Jarrett et al. 2000), and SDSS DR8

main sample galaxies (Aihara et al. 2011). Significant correlation (at the level of 3–5σ) was observed at small angular scales, $\lesssim 1°$, for all of the catalogs except the Luminous Red Galaxies, and the results are interpreted in terms of constraints on the composition of the UGRB. This work updates these analyses in several aspects: (1) We use a larger amount of *Fermi* data, almost 7 years compared to 5 years. In doing so, we employ the new *Fermi*-LAT Pass 8 data selection (Atwood et al. 2013), based on an improved event reconstruction algorithm and providing a $\sim$30% larger effective area. The full Pass 8 data set is roughly two times larger than the 5-year Pass 7 data set. With such a large data set, we can perform our cross-correlation analysis in more energy bins. We now consider up to eight energy bins instead of the three used in X15. (2) We use updated versions of the original galaxy catalogs. For example, we now use the 2MASS Photometric Redshift catalog (2MPZ) instead of 2MASS. 2MPZ extends the 2MASS data set by adding precise photometric redshifts that were not available before (but see Jarrett 2004). Thanks to this, we can perform a cross-correlation analysis, subdividing the sample into a number of different *z* bins. Similarly, instead of the SDSS main sample galaxies, we now consider the latest SDSS DR12 photometric galaxy catalog. As for the NVSS catalog and the QSO sample, we consider the same data sets used in the previous analyses. (3) We consider a new data set: the *WISE* $\times$ SuperCOSMOS photometric redshift catalog (WI$\times$SC; Bilicki et al. 2016). This is a natural extension of 2MPZ, providing coverage of $\sim$75% of the sky and reaching in redshift up to almost $z \sim 0.5$.

In our analysis, we will use the same methodology as in X15 and estimate the angular two-point cross-correlation function (CCF) and the cross-angular power spectrum (CAPS) of the UGRB maps and discrete object catalogs. The rationale for computing two quantities, CCF and CAPS, that contain the same information is that they are largely complementary since their estimates are affected by different types of biases and, which is probably more important, the properties of the error covariance are different in the two cases.

The layout of the paper is as follows. In Section 2 we present the *Fermi*-LAT maps and their accompanying masks and discuss the procedure adopted to remove potential spurious contributions to the extragalactic signal. In Section 3 we present the catalogs of different types of extragalactic sources that we cross-correlate with the *Fermi* UGRB maps. In Section 4 we briefly describe the CCF and CAPS estimators and their uncertainties. In Section 5 we propose a simple, yet physically motivated, model for the cross-correlation signal and introduce the χ^2 analysis used to perform the comparison with the data. The results of the cross-correlation analysis are described in Section 6 and discussed in Section 7, in which we also summarize our main conclusions. An extended discussion of the systematic errors is presented in Appendix A, where we describe the results of a series of tests to assess the robustness of our results. Appendix B contains additional plots that show results of the cross-correlation analysis not included in the main text.

To model the expected angular cross-correlations, we assume a flat, cold DM model with a cosmological constant (ΛCDM) with cosmological parameters $\Omega_b h^2 = 0.022161$, $\Omega_c h^2 = 0.11889$, $\tau = 0.0952$, $h = 0.6777$, $\ln 10^{10} A_s = 3.0973$ at $k_0 = 0.05$ Mpc^{-1}, and $n_s = 0.9611$, in accordance with the most recent Planck results (Planck Collaboration et al. 2016).

The data files containing the results of our cross-correlation analysis are publicly available at https://www-glast.stanford.edu/pub_data/.

2. *Fermi*-LAT Maps

In this section, we describe the EGB maps obtained from 7 years of *Fermi*-LAT observations and the masks and procedures used to subtract contributions from (1) γ–ray resolved sources, (2) Galactic diffuse emission due to interaction of cosmic rays with the interstellar medium, and (3) additional Galactic emission located high above the Galactic plane in prominent structures such as the Fermi Bubbles (Su et al. 2010) and Loop I (Casandjian et al. 2009).

Fermi-LAT is a pair-conversion telescope on board the *Fermi* Gamma-ray Space Telescope (Atwood et al. 2009). It covers the energy range between 20 MeV and $\sim$1 TeV, most of which will be used in our analysis ($E = [0.25, 500]$ GeV), and has an excellent angular resolution ($\sim 0°\!.1$ above 10 GeV over a large field of view ($\sim$2.4 sr).

For our study, we have used 78 months of data from 2008 August 4 to 2015 January 31 (*Fermi* Mission Elapsed Time 239,557,418–444,441,067 s), considering the Pass 8 event selection (Atwood et al. 2013) and excluding photons detected with measured zenith angle larger than 100° to reduce the contamination from the bright Earth limb emission. We used both back-converting and front-converting events. The corresponding exposure maps were produced using the standard routines from the LAT *Science Tools*[9] version 10-01-01 and the P8R2_CLEAN_V6 instrument response functions (IRFs). We have also used for a cross-check the P8R2_ULTRACLEAN-VETO_V6 IRFs, which provide a data selection where residual contamination of the γ-ray sample from charged cosmic rays is substantially reduced, at the price of a decrease in effective area of $\sim$30%. To pixelate the photon counts, we have used the GaRDiAn package (Ackermann et al. 2009, 2012b). The count maps were generated in HEALPix[10] format (Górski et al. 2005) containing $N_{pix} = 12,582,912$ pixels with mean spacing of $0°\!.06$, corresponding to the HEALPix resolution parameter $N_{side} = 1024$.

Thanks to the large event statistics, we consider eight bins with energy edges $E = 0.25, 0.5, 1, 2, 5, 10, 50, 200$, and 500 GeV. In several cases we have grouped the events in three wider intervals in order to have better statistics and higher signal-to-noise ratio: $0.5 < E < 1$ GeV, $1 < E < 10$ GeV, and $10 < E < 200$ GeV.

The masking, the cleaning procedure, and the tests aimed at assessing our ability to remove contributions from the Galactic foreground and resolved sources have been described in detail in Xia et al. (2011) and in X15. Here we summarize the main steps.

(1) The geometry mask excludes the Galactic Plane $|b| < 30°$, the region associated with the Fermi Bubbles and the Loop I structure, and two circles of 5° and 3° radius at the position of the Large and Small Magellanic Clouds, respectively. The 500 brightest point sources (in terms of the integrated photon flux in the 0.1–100 GeV energy range) from the 3FGL catalog are masked with a disk of radius 2°, and the remaining ones with a disk of 1° radius. We notice that in several of the cross-correlation analyses (in particular the ones

---

[9] http://fermi.gsfc.nasa.gov/ssc/data/analysis/documentation/Cicerone/
[10] http://healpix.jpl.nasa.gov/

involving SDSS-related catalogs) presented below, the mask of the catalog largely overlaps and sometimes includes the *Fermi* one, so the effective geometry mask used is more conservative than the one described here.

(2) The Galactic diffuse emission in the unmasked region has been removed by subtracting the model `gll_iem_v05_rev1.fit`[11] (Acero et al. 2016) from the observed emission. More precisely, in the unmasked region, we performed, separately in each energy bin, a two-component fit including the Galactic emission from the model above and a purely isotropic emission. Convolution of the two template maps with the IRFs and subsequent fit to the observed counts were then performed with GaRDiAn. The best-fit isotropic plus Galactic emission, in count units, was then subtracted off from the γ-ray count maps, and finally divided by the exposure map in the considered energy range to obtain the residual flux maps used for the analysis. The robustness of this cleaning procedure has been tested against a different Galactic diffuse emission model, `ring_2year_P76_v0.fits` (see footnote 11). We have found that the two models are very similar in our region of interest. As a result, their residuals agree at the percent level. We stress, nonetheless, that the Galactic foregrounds are not expected to correlate with extragalactic structures, and thus it is not crucial to achieve a *perfect* cleaning. Indeed, in X15, we did show that, even without foreground removal, the recovered cross-correlations were unbiased, while the main impact of foreground removal was to suppress the background and thus to reduce the size of the random errors. Similar conclusions were reached in the recent cross-correlation analysis of weak lensing catalogs with *Fermi*-LAT performed by Tröster et al. (2017). Analogous considerations apply to the point sources. Especially at low energies, some leakage of the point sources outside the mask is expected, since the point-spread function (PSF) of the instrument becomes large and the tails lie outside the mask. Nonetheless, bright point sources should not correlate with extragalactic sources, so the leakage is expected to increase the random noise but not to introduce biases. In Appendix A, we test the validity of this assumption by estimating the correlation using different point-source masks and find that the results are insensitive to the choice of the mask.

(3) An imperfect cleaning procedure may induce spurious features in the diffuse γ-ray signal on large angular scales. These should not significantly affect our cross-correlation analysis since they are not expected to correlate with the sources responsible for the UGRB. Nevertheless, to minimize the chance that spurious large-scale correlation power may leak into the genuine signal, we performed an additional cleaning step (dubbed $\ell 10$ cleaning) and removed contributions up to multipoles $\ell = 10$, including the monopole and dipole, from all of the maps, using standard HEALPix tools. This cleaning procedure was also adopted in Xia et al. (2011).

Example maps are shown in Figure 1 for the energy range 1–10 GeV, with and without the fiducial mask, and after the foreground subtraction and $\ell 10$ cleaning. In the bottom panel, the residuals are shown without the Bubbles/Loop I mask in order to show that the cleaning works well nonetheless also in this region.
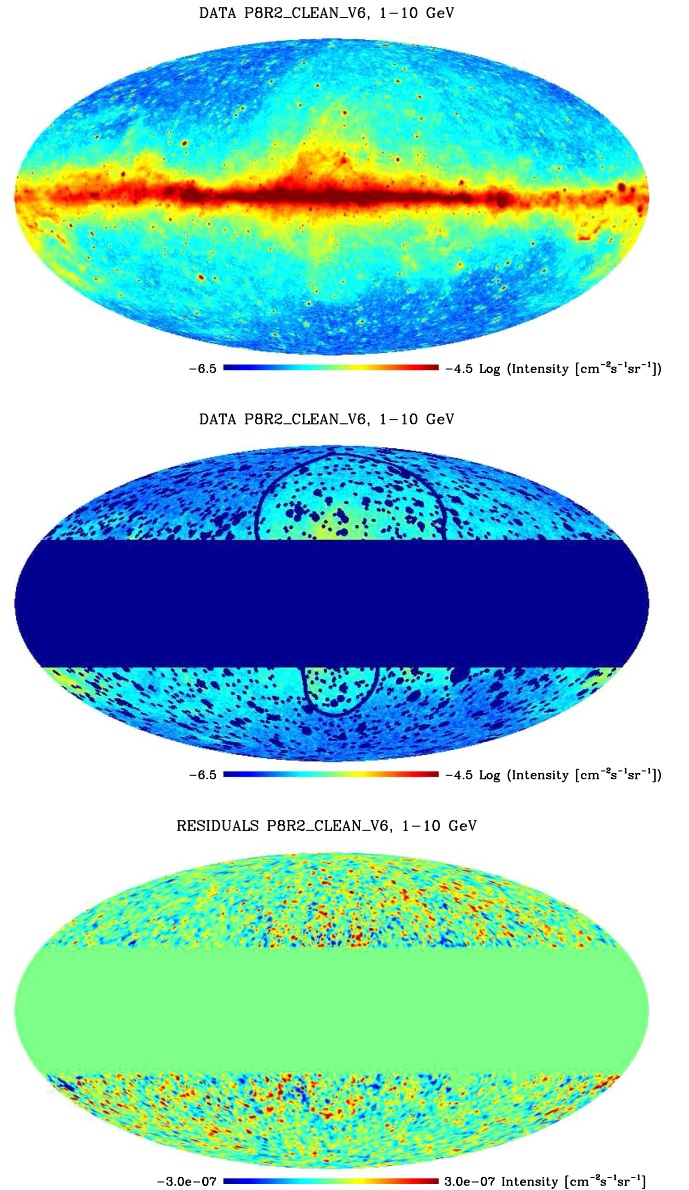
Figure 1. All-sky Mollweide projections of *Fermi*-LAT total flux maps in the energy range 1–10 GeV. Upper panel: flux map without mask. Middle panel: flux map together with the fiducial mask, covering 3FGL point sources and the Galactic $|b| < 30°$ region. The two further visible lines enclose the region covering the *Fermi* Bubbles and the Loop I area. Lower panel: residual flux maps after Galactic foreground subtraction and $\ell 10$ cleaning. For better visualization, the upper two maps have been smoothed with a Gaussian beam of FWHM = $0°\!.5$, and the lower one with FWHM = $1°$.

3. Catalogs of Discrete Sources

In this work, we use five different catalogs of extragalactic objects for the cross-correlation analysis. They span wide, overlapping redshift ranges, contain different types of objects (galaxies, quasars) detected at several wavelengths (UV, optical, near- and mid-infrared, radio) whose distances, when available, are inferred from photometric redshifts. They all share two important characteristics: large angular coverage to maximize the number of Fourier modes available to the cross-correlation analysis, and a large number of objects to minimize shot noise errors. The redshift distributions of the sources in the various catalogs are shown in Figure 2. Overall, they span an extended range of redshift, from $z = 0$ out to $z \sim 5$. Such a
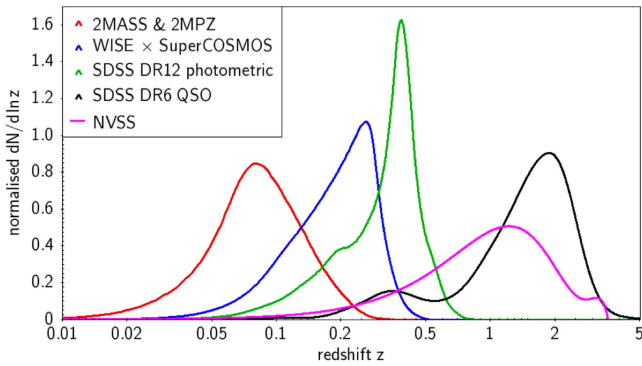
Figure 2. Redshift distributions of the five data sets used in our analysis. The curves show their normalized dN/dz distributions, based on photometric redshifts of the sources. An exception is the NVSS, where no redshift estimates are available, so the analytical approximation described in the text was assumed.

Table 1
Statistics of the Source Catalogs Used for the Cross-correlation

Source Catalog	Sky Coverage	Number of Sources	Mean Surface Density (deg^{-2})
NVSS	25.5%	177, 084	16.8
2MPZ	28.8%	293, 424	24.7
WISE × SCOS	28.7%	7, 544, 862	638
SDSS DR12	12.3%	15, 194, 640	2980
SDSS DR6 QSO	11.7%	340, 162	70.3

Note. The sky coverage indicates the area effectively used in the analysis, i.e., after applying both the catalog and γ-ray masks. The numbers refer to the objects contained in the selected regions.

wide redshift coverage is of paramount importance to identifying the nature of the UGRB that could be generated both by nearby (SFGs and DM annihilation processes in halos) and high-redshift sources (e.g., blazars). In Table 1 we summarize the basic properties of the source catalogs used in our analysis, such as their sky coverage, source number, and mean surface density of the objects in the region of sky effectively used for the analysis, that is, after applying both the catalog and γ-ray masks. In the following sections, instead, when describing a given catalog, we will report numbers referring to the nominal mask of the catalog itself.

3.1. NVSS

The NRAO VLA catalog (NVSS, Condon et al. 1998) is the largest catalog of radio sources currently available. The sample considered in our analysis contains $\sim 5.7 \times 10^5$ objects with a flux >10 mJy, located at declinations $\delta \gtrsim -40°$ and outside a relatively narrow Zone of Avoidance ($|b| > 5°$). The mean surface density of sources is ~ 16.9 deg^{-2}. This is the same NVSS data set used in the cross-correlation analysis of X15. The map showing the sky coverage and angular positions of the objects can be found in Xia et al. (2011, Figure 9).

The main reason for repeating the cross-correlation analysis using the new Pass 8 *Fermi* data is to check the robustness of the strong correlation signal at small angular separation found by X15 and interpreted as being contributed by the same NVSS galaxies emitting in gamma rays.

Radio sources in the NVSS catalog do not come with an estimate of their redshift. We use the redshift distribution determined by Brookes et al. (2008). Their sample, contained 110 sources with $S > 10$ mJy, of which 78 (71% of the total) had spectroscopic redshifts, 23 had redshift estimates from the K–z relation for radio sources, and nine were not detected in the K band and therefore had a lower limit to z. We adopt the smooth parameterization of this distribution given in de Zotti et al. (2010), shown in Figure 2 with the magenta line.

3.2. SDSS DR6 QSO

In recent years, several quasar catalogs have been obtained based on the SDSS data set, complemented in some cases with additional information, most notably from the *Wide-field Infrared Survey Explorer* (*WISE*). They all are meant to supersede the SDSS DR6 QSO catalog (Richards et al. 2009,

hereafter DR6 QSO) used in the previous cross-correlation analyses by Xia et al. (2011, 2015). We checked the adequacy of these new samples using two criteria: the surface number density of objects, which has to be large to minimize the shot noise error, and the uniformity in the selection function of the catalog across the sky to ensure a uniform calibration of the catalog. Our tests have shown that none of the newer data sets satisfy these requirements better than the original DR6 QSO since in all of the new samples we detected large variations in the number density of sources across the sky. Neither aggressive cleaning procedures nor geometry cuts were able to guarantee angular homogeneity without heavily compromising the surface density of sources.

For these reasons, we decided to rely on the original DR6 QSO catalog. We applied the same preselection procedures as in Xia et al. (2011, 2015). In particular, we considered only the sources with an UV excess flag uvxts = 1, since this criterion provides a uniform selection. There are about 6×10^5 sources in the sample selected this way, covering $\sim 25\%$ of the sky, with photometric redshifts $0 < z < 5.75$ ($\langle z \rangle \simeq 1.5$) of typical accuracy $\sigma_z \sim 0.24$. Figure 2 shows the smoothed dN/dz of this data set (black line). We note, however, that the original histogram as derived from the Richards et al. (2009) data is very nonuniform, exhibiting multiple peaks (see, e.g., Figure 1 in Xia et al. 2009), probably an artifact of the photo-z assignment method. Nevertheless, this is of minor importance for the present paper, as for the cross-correlation we use very broad redshift shells. In particular, we split the DR6 QSO data set into three bins of $z \in [0.0, 1.0]$, $[1.0, 2.0]$, and $[2.0, 4.0]$, selected in a way to have a similar number of objects in each bin. The use of redshift shells is, together with the updated *Fermi* data and binning in energy, a novel element of the QSO–γ-ray cross-correlation analysis in comparison to Xia et al. (2011, 2015), where the same quasar sample was considered as one broad bin encompassing all of the data. Figure 3 shows all-sky projections of the three redshift shells of the DR6 QSO catalog in HEALPix format. We have excluded from the analysis the three narrow stripes present in the south Galactic sky and use only the northern region.

3.3. 2MPZ

The 2MPZ (Bilicki et al. 2014) is a data set of galaxies with measured photometric redshifts constructed by cross-matching three all-sky data sets covering different energy bands: 2MASS-XSC (near-infrared, Jarrett et al. 2000), *WISE* (mid-infrared, Wright et al. 2010), and SuperCOSMOS scans of UKST/POSS-II photographic plates (optical, Peacock et al. 2016).
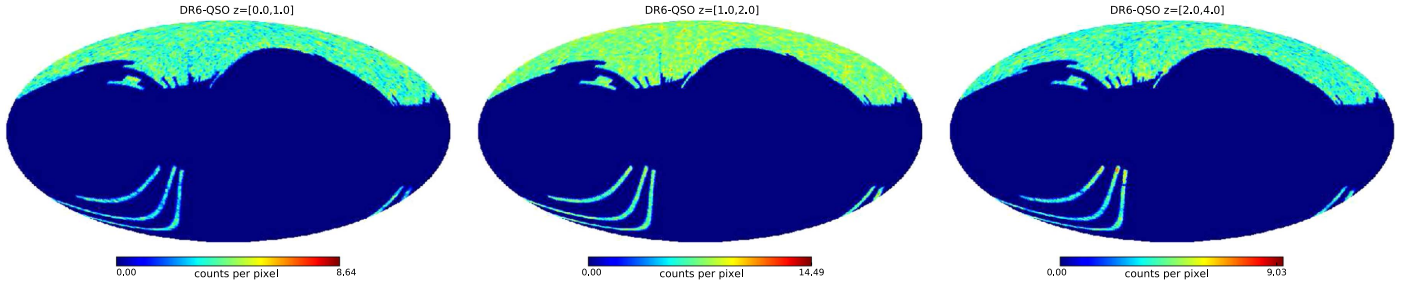
Figure 3. All-sky projections of the SDSS DR6 QSO distribution in the three redshift shells adopted in the analysis. The maps have HEALPix resolution $N_{side} = 128$ and include additional Gaussian smoothing of FWHM $= 1°$ for better visualization.
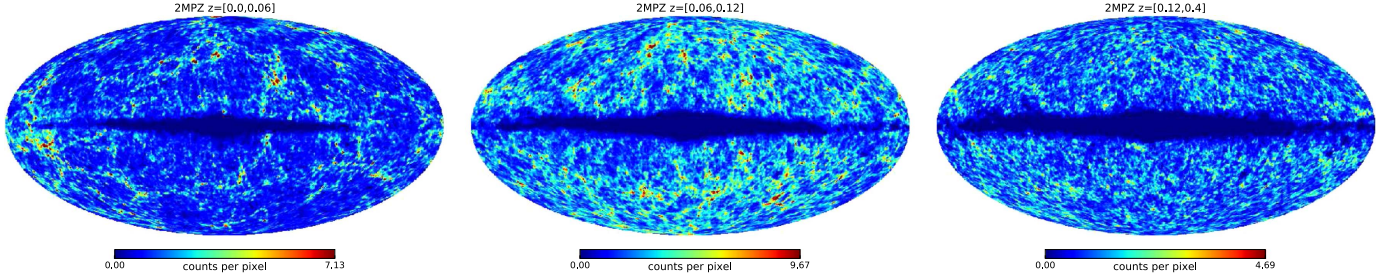

Figure 4. All-sky projections of the 2MPZ galaxy distribution in the three redshift shells adopted in the analysis. The maps have HEALPix resolution $N_{side} = 128$ and include additional Gaussian smoothing of FWHM $= 1°$ for better visualization.

2MPZ is flux limited at $K_s < 13.9$ and contains $\sim$935,000 galaxies over most of the sky. However, since the strip at $|b| < 10°$ is undersampled, in our analysis we masked out this region as well as other incompleteness areas, using a mask similar to the one shown in Alonso et al. (2015).

The 2MPZ photo-z values are generally unbiased ($\langle \delta z \rangle \sim 0$). Their random errors are almost distance-independent, and their distribution has an rms scatter $\sigma_z = 0.015$ with 1% of outliers beyond $3\sigma_z$. The redshift distribution of 2MPZ galaxies is shown in Figure 2 (red line). It peaks at $z \sim 0.06$ and has $\langle z \rangle \sim 0.08$. The surface density of objects is $\sim$30 sources per square degree. 2MPZ is the only wide catalog that comprehensively probes the nearby universe ($z \lesssim 0.2$) all-sky and has reliable redshift estimates. This feature and the possibility of dividing the sample into different redshift shells are crucial to constraining the composition of the UGRB. For our analysis, we split the catalog into three redshift bins: $z \in [0.00, 0.06]$, $[0.06, 0.12]$, and $[0.12, 0.40]$. The binning was designed to bracket the mean redshift in the second bin and to guarantee a reasonably large number of objects in the two other bins. Moreover, this binning has a good overlap with that adopted to slice the SDSS DR12 sample (Section 3.5). In Section 6.3 we shall also use the full 2MPZ sample for the cross-correlation analysis (the case dubbed "ZA") so that the results can be directly compared with those of X15, obtained using the 2MASS catalog.

The all-sky distribution of 2MPZ galaxies in each of the three redshift bins is shown in Figure 4.

3.4. WISE× SuperCOSMOS

The WISE $\times$ SuperCOSMOS photometric redshift catalog (Bilicki et al. 2016), hereafter WI×SC, is the result of cross-matching the two widest galaxy photometric catalogs currently available: the mid-infrared WISE and optical SuperCOSMOS data sets. Information from GAMA-II (Liske et al. 2015) and SDSS DR12 (Alam et al. 2015) was used to exclude stars and quasars, to obtain a sample of $\sim$20 million galaxies with a

mean surface density above 650 sources per square degree. The resulting catalog is $\sim$95% pure at high Galactic latitudes of $|b| > 30°$ and highly complete over $\sim$70% of the sky, outside the Zone of Avoidance ($|b| < 10°$ plus the area around the Galactic bulge) and other confusion regions.

Photometric redshifts for all galaxies, calibrated on GAMA-II, were estimated with a systematic error $|\delta_z| \sim 10^{-3}$ and a random error $\sigma_z \sim 0.033$ with $\sim$3% of outliers beyond $3\sigma_z$. The redshift distribution of WI×SC galaxies has a mean $\langle z \rangle = 0.2$ and is characterized by a broad peak extending from $z \sim 0.1$ to $z \sim 0.3$ and a prominent high-z tail reaching up to $z > 0.4$, as shown in Figure 2 (blue curve).

After masking, we are left with about 18.5 million galaxies that we divided into four redshift bins: $z \in [0.00, 0.09]$, $[0.09, 0.21]$, $[0.21, 0.30]$, and $[0.30, 0.50]$. As in the 2MPZ case, the binning was chosen to guarantee a significant overlap with the other source catalogs used in our analysis. The first bin, Z1, encompasses the first two redshift bins of the 2MPZ sample, as well as the first redshift bin of the SDSS DR12 one. Because of the bright cut used to build the catalog, WI×SC probes an intrinsically faint population and has very few sources in common with 2MPZ and SDSS DR12 at $z \lesssim 0.09$ (for more details, see Bilicki et al. 2016). The two bins at $z > 0.21$, which contain an approximately equal number of WI×SC galaxies, overlap with SDSS DR12 bins Z3 (i.e., the third redshift bin) and Z4+Z5.

The sky maps of the WI×SC sources in the four bins are shown in Figure 5. The problematic areas near the Galaxy and the Magellanic Clouds, which feature prominently especially in the first bin, have been masked out and excluded from the cross-correlation analysis. A residual overdensity of sources along the Galactic Plane, which is visible in the first and last redshift bin and is likely due to stellar contamination, survives the masking procedure. We decided to remove it by applying the same $\ell 10$ cleaning procedure as adopted for the γ-ray map. This conservative procedure has little impact on the cross-correlation analysis since these problematic areas are largely
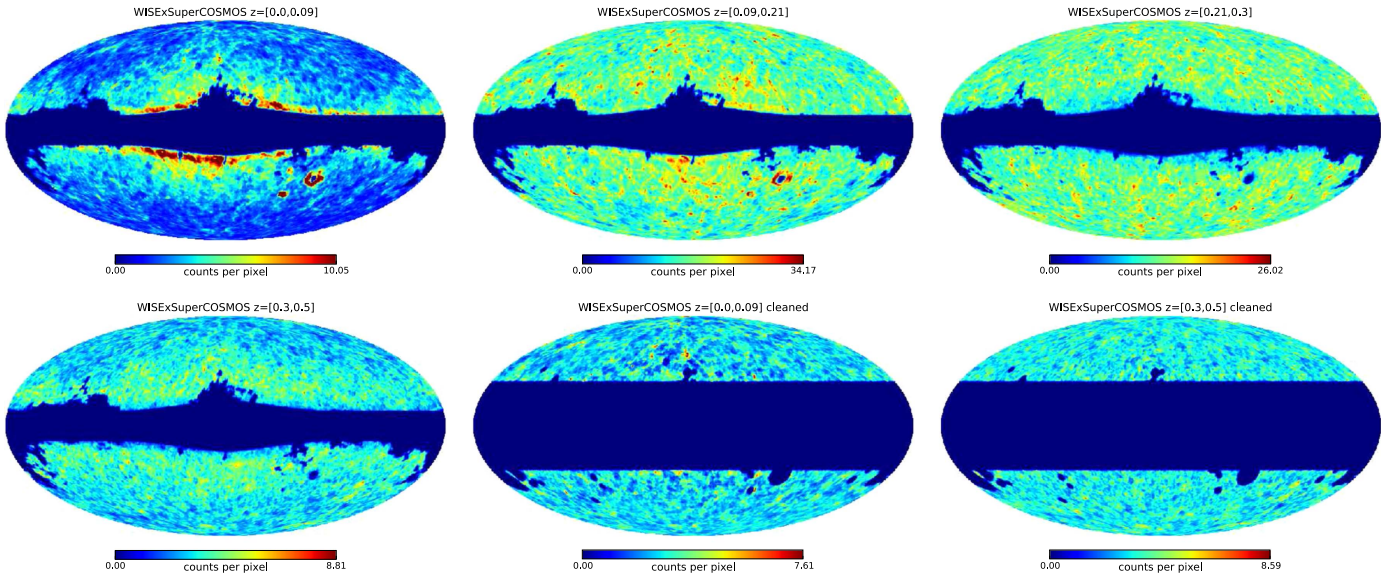
Figure 5. All-sky projections of the *WISE* × SuperCOSMOS galaxy distribution in the four redshift shells adopted in the analysis. The maps have HEALPix resolution $N_{side} = 256$ and include additional Gaussian smoothing of FWHM $= 1°$ for better visualization. The two bottom-right panels show the first and the last redshift bins after the $\ell10$ cleaning procedure and applying the catalog mask and the fiducial Galactic plane mask of $|b| < 30°$.

excluded by the *Fermi* Galactic plane mask ($|b| < 30°$), which we apply in each cross-correlation (see, e.g., the bottom right panels of Figure 5).

3.5. SDSS DR12 Photometric

This catalog is a revised version of the one used in Xia et al. (2011, 2015). It has been derived from the SDSS photometric redshift catalog of Beck et al. (2016), which includes over 200 million sources classified by SDSS as galaxies, and provides photometric redshifts for a large part of them. Following authors' recommendations,[12] we considered only the sources with a photometric error class -1, 1, 2, or 3, whose rms redshift error is $\sigma_z \leqslant 0.074$ (Beck et al. 2016). This data set was further purified to obtain a uniform depth over the observed area. For that reason, we considered only galaxies with extinction-corrected r-band magnitudes in the range $13 < r < 21$ outside the Zone of Avoidance $-10° < b < 15°$, as well as areas of r-band extinction $A_r < 0.18$. After applying these selection criteria, we are left with 32 million sources with a mean redshift $\langle z \rangle = 0.34$ and mostly within $z < 0.6$. The sky coverage is $\sim27\%$, and the mean surface density is $\sim2900 \deg^{-2}$. As shown in Figure 2 (green line), their redshift distribution features a main peak at $z \sim 0.38$ and a secondary one at $z \sim 0.19$, possibly indicating some issue with the photo-z assignment. Given the very large density of objects, we can split the sample into several redshift bins, keeping low shot noise in each shell. In our analysis, we divided the data set into seven redshift bins: six of width $\Delta z = 0.1$, starting from $z = 0$ to $z = 0.6$, and the seventh encompassing the wider range $0.6 < z < 1$ (to compensate for the source fall-off in the redshift distribution). These shells are illustrated in all-sky maps in Figure 6. It can be seen that the SDSS galaxies are distributed into two disconnected regions in the Galactic south and north, with most of the area in the north part. Furthermore, as shown in the figure, the southern region has quite uneven sampling. For this reason, we have excluded this region from the analysis and use only the northern part.

4. Cross-correlation Analysis

In the previous section, we have presented the catalogs of extragalactic objects that we use in the analysis. Their format is that of a 2D pixelated map of object counts $n(\hat{\Omega}_i)$, where $\hat{\Omega}_i$ specifies the angular coordinate of the ith pixel. For the cross-correlation analysis, we consider maps of normalized counts $n(\hat{\Omega}_i)/\bar{n}$, where $\bar{n}$ is the mean object density in the unmasked area, and the *Fermi*-LAT residual flux sky maps, also pixelated with a matching angular resolution.

In our analysis, we compute both the angular two-point cross-correlation function (CCF), $w^{(\gamma c)}(\theta)$, and its harmonic transform, the angular power spectrum $\bar{C}_\ell^{(\gamma c)}$, CAPS. In particular, we shall use the CCF for visualization purposes, but we restrict the quantitative analysis to the CAPS only. The reason for this choice is that CAPS has the advantage that the different multipoles are almost uncorrelated, especially after binning. Their covariance matrix is therefore close to diagonal, which simplifies the comparison between models and data. Furthermore, it is easier to subtract off instrumental effects like the PSF smearing, since a convolution in configuration space is just a multiplicative factor in harmonic space. On the other hand, its interpretation is not so intuitive since the CAPS signal typically extends over a broad range of multipoles. The CCF offers the advantage of a signal concentrated within a few degrees that can be intuitively associated with the angular size of the γ-ray-emitting region. The quantitative analysis of the CCF is, instead, more challenging because the cross-correlation signals in different angular bins are highly correlated and the PSF convolution effect is more difficult to account for.

Following X15, we use the *PolSpice*[13] statistical tool kit (Szapudi et al. 2001; Chon et al. 2004; Efstathiou 2004a; Challinor & Chon 2005) to estimate both CCF and CAPS. *PolSpice* automatically corrects for the effect of the mask. In this respect, we point out that the effective geometry of the mask used for the correlation analysis is obtained by combining that of the LAT maps with those of each catalog of

---

[12] See also http://www.sdss.org/dr12/algorithms/photo-z/.

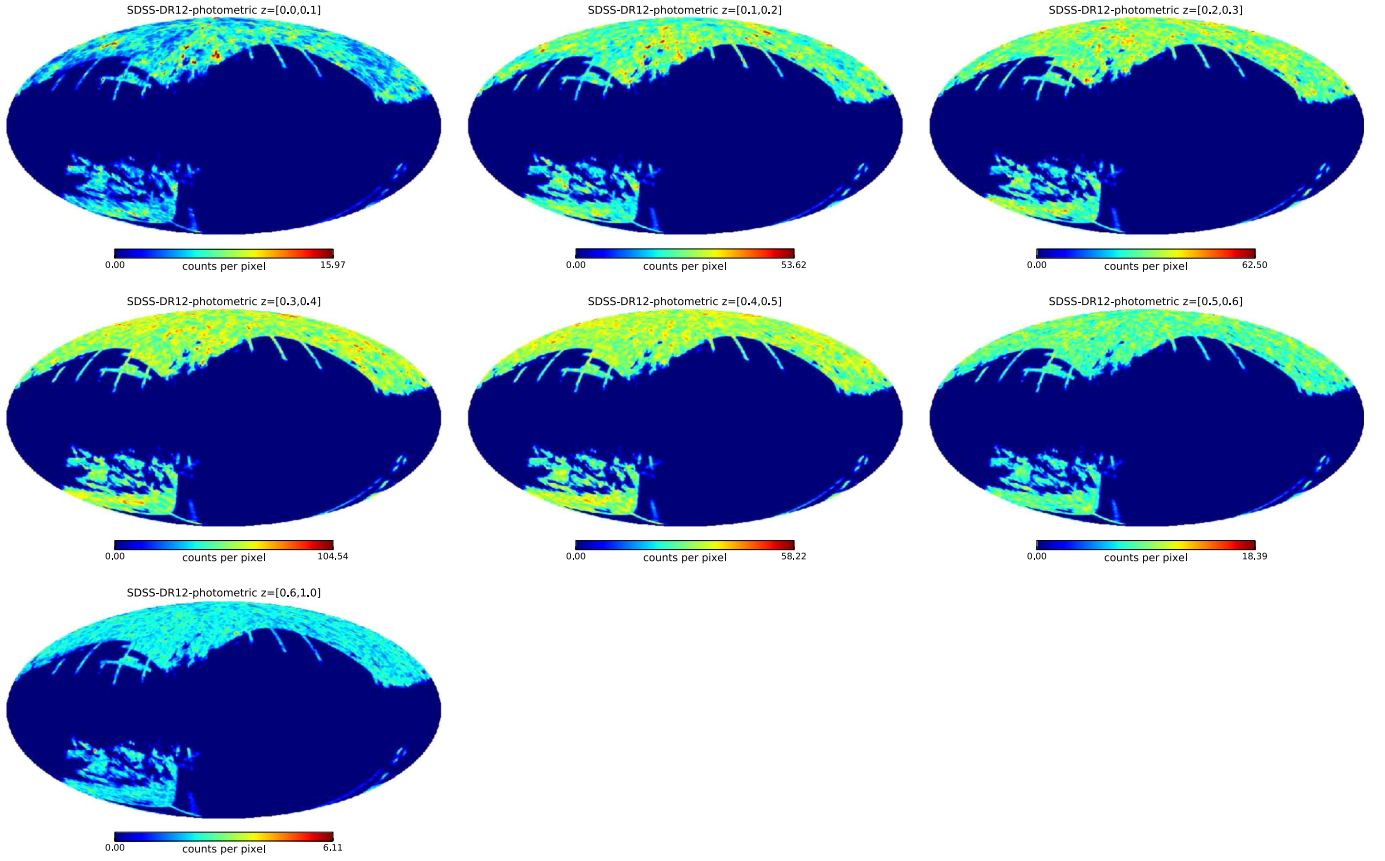[13] See http://www2.iap.fr/users/hivon/software/PolSpice/.

Figure 6. All-sky projections of the SDSS DR12 photometric galaxy distribution in the seven redshift shells adopted in the analysis. The maps have HEALPix resolution $N_{\mathrm{side}} = 256$ and include additional Gaussian smoothing of FWHM $= 1°$ for better visualization.

astrophysical objects. The accuracy of the *PolSpice* estimator has been assessed in X15 by comparing the measured CCF with the one computed using the popular Landy–Szalay method (Landy & Szalay 1993). The two were found to be in very good agreement. *PolSpice* also provides the covariance matrix for the angular power spectrum, $\bar{V}_{\ell\ell'}$ (Efstathiou 2004b).

The instrument PSF and the map pixelation affect the estimate of the CAPS. To remove these effects, we proceed as in X15: we first derive the beam window function W_ℓ^B associated with the LAT PSF and the pixel window function W_ℓ^{pixel} associated with the map pixelation. Since the LAT PSF varies significantly with energy, we derive W_ℓ^B on a grid of 100 energy values from 100 MeV to 1 TeV. This is then used to derive the average W_ℓ^B in the specific energy bin analyzed. The procedure is described in detail in X15. Then we exploit the fact that convolution in configuration space is a multiplication in harmonic space and estimate the deconvolved CAPS $C_\ell^{(\gamma c)}$ from the measured one $\bar{C}_\ell^{(\gamma c)}$ as $C_\ell^{(\gamma c)} = (W_\ell)^{-1} \bar{C}_\ell^{(\gamma c)}$, where $W_\ell = W_\ell^B (W_\ell^{\mathrm{pixel}})^2$ is the global window function. The window function W_ℓ has two contributions, from the LAT and cross-correlating catalog: it is the double product of the beam window W_ℓ^B and the pixelation window function W_ℓ^{pixel} from each catalog. However, we neglect a factor of W_ℓ^B related to the catalog maps since the typical angular resolution of the catalogs ($<10''$) is much smaller than the pixel size, so the associated $W_\ell^B \simeq 1$. The square in the W_ℓ^{pixel} term takes into account the pixel window functions of both maps. Its effect is minor since, as shown in Figure 3 in Fornasa et al. (2016), its value is close to unity up to $\ell = 2000$, which is the maximum multipole considered in our analysis. The covariance

matrix for the deconvolved $C_\ell^{(\gamma c)}$ is then expressed as $V_{\ell\ell'} = \bar{V}_{\ell\ell'} W_\ell^{-2} W_{\ell'}^{-2}$. Finally, to reduce the correlation in nearby multipoles induced by the angular mask, we bin the measured CAPS into 12 equally spaced logarithmic intervals in the range $\ell \in [10, 2000]$. We choose logarithmic bins to account for the rapid loss of power at high ℓ induced by the PSF. We indicate the binned CAPS with the same symbol as the unbinned one, $C_\ell^{(\gamma c)}$. It should be clear from the context which one is used. The $C_\ell^{(\gamma c)}$ in each bin is given by the simple unweighted average of the $C_\ell^{(\gamma c)}$ within the bin. For the binned $C_\ell^{(\gamma c)}$, we build the corresponding covariance matrix as a block average of the unbinned covariance matrix, that is, $\sum_{\ell\ell'} V_{\ell\ell'}/\Delta\ell/\Delta\ell'$, where $\Delta\ell$, $\Delta\ell'$ are the widths of the two multipole bins, and ℓ, ℓ' run over the multipoles of the first and the second bin. The binning procedure is very efficient in removing correlation among nearby multipoles, resulting in a block covariance matrix that is, to a good approximation, diagonal.[14] For this reason, we will neglect the off-diagonal terms in our analysis and only use the diagonal ones: $(\Delta C_\ell)^2 = \sum_{\ell\ell'} V_{\ell\ell'}/\Delta\ell^2$.

---

[14] Note that, in the case of non-Gaussian fluctuations, like the one considered here, the nonvanishing trispectrum could induce, possibly, extra correlation among the multipoles (Komatsu & Seljak 2002; Ando et al. 2017). These terms are not considered in the covariance matrix computed by *PolSpice*, which we use in our analysis. The importance of these terms for our analysis is uncertain, although we have found that errors computed using the *PolSpice* covariance matrix are compatible with those computed using Jackknife resampling techniques (X15). A dedicated analysis would be required to properly quantify the impact of these terms, which is beyond the scope of this work.

The CCF covariance matrix can be computed from the CAPS covariance as (Planck Collaboration et al. 2014)

$$C_{\theta\theta'}^{PS} = \sum_\ell \sum_{\ell'} \frac{2\ell+1}{4\pi} \frac{2\ell'+1}{4\pi} P_\ell(\cos\theta) P_{\ell'}(\cos\theta') \bar{V}_{\ell\ell'}. \quad (1)$$

An average over the angular separations θ and θ' within each bin can be performed to obtain a binned covariance matrix. In the following, we will compute the $w^{(\gamma c)}(\theta)$ in the range $\theta \in [0°.1, 100°]$ binned into 10 logarithmically spaced bins. Since, as already mentioned, we limit our quantitative analysis to CAPS, we shall not use the CCF covariance matrix nor make any attempt to deconvolve the measured $w^{(\gamma c)}(\theta)$ to account for the effects of the PSF and pixelation. We do, however, show the measured CCF and its errors in our plots. The error bars there correspond to the diagonal element of the binned CCF covariance matrix. Error covariance is therefore not represented in the plots.

5. CAPS Models and χ^2 Analysis

In this section, we illustrate our models for the CAPS and the CCF and how we compare them with the measurements.

We consider a simple, phenomenological CAPS model, inspired by the *halo model* (Cooray & Sheth 2002), in which the angular spectrum in each energy bin is a sum of two terms:

$$\hat{C}_\ell^{\gamma c} = C^{1h} + A^{2h} C_\ell^{2h}, \quad (2)$$

named 1-halo and 2-halo terms, respectively. The halo model assumes that all matter in the universe is contained in DM halos populated by baryonic objects, like galaxies, AGNs, and, in particular, γ-ray sources. In this framework, C^{1h} quantifies the spatial correlation within a single halo, that is, γ-ray sources and extragalactic objects that reside in the same DM halo. The special case in which the γ-ray and the extragalactic sources are the same object detected at different wavelengths is, sometimes, treated differently, since it formally corresponds to a Dirac-delta correlation in real space. Nonetheless, since halos are typically smaller than the available angular resolution of *Fermi*-LAT, it is, in practice, hard to distinguish the degenerate case from the case of two separate objects Thus, for simplicity, we include both in a single term that contributes to the 1-halo correlation. The C^{2h} term describes the halo–halo clustering. If nonzero, it indicates that both γ-ray sources and extragalactic objects trace the same large-scale structure.

The Fourier transform of the 1-halo term C^{1h} is therefore made of two components. The first one, which comes from the Dirac delta, is a constant term in the ℓ space. The second one, which is the Fourier transform of the halo profile, does depend on the multipole ℓ. In practice, however, its ℓ dependence is very weak because DM halos are almost point-like at the resolution set by the LAT PSF. Therefore, we model the total C^{1h} as a constant and ignore any multipole dependence. We believe that this is a fair hypothesis for all analyses performed in this study except, perhaps, the cross-correlation with the 2MPZ catalog since some of the halo hosts are close enough to us to appear wider than the LAT PSF. In this case, the modeling of C^{1h} is probably inaccurate at the highest ℓ. Nonetheless, this inconsistency should have a negligible impact on our analysis because of the large errors on the C_ℓ measured at large multipoles, which reduce substantially the sensitivity to the

shape of the C^{1h} at high ℓ values. The second free parameter of the model is A^{2h}, which sets the amplitude of the 2-halo term, C_ℓ^{2h}, that accounts for the correlation among halos. Its ℓ dependence reflects the angular correlation properties of the DM halo distribution. To a first approximation it can be expressed as

$$C_\ell^{2h} = \frac{2}{\pi} \int k^2 P(k) [G_\ell^\gamma(k)] [G_\ell^c(k)] dk, \quad (3)$$

where $P(k)$ is the power spectrum of matter density fluctuations. We take the linear prediction of $P(k)$ from the *camb* code (Lewis et al. 2000) for the Planck Collaboration et al. (2016) cosmological parameters specified in Section 1, and we apply a nonlinear correction using *halofit* (Smith et al. 2003; Takahashi et al. 2012). The functions $G(k)$ specify the contribution of each field to the cross-correlation signal. More specifically, the contribution from the field of number density fluctuations in a population of discrete objects is given by

$$G_\ell^c(k) = \int \frac{dN}{dz} b_c(z) D(z) j_\ell[k\chi(z)] dz, \quad (4)$$

where dN/dz is the redshift distribution of the objects, j_ℓ are spherical Bessel functions, $D(z)$ is the linear growth factor of density fluctuations, b_c is the linear bias parameter of the objects, and $\chi(z)$ is the comoving distance to redshift z. The analogous quantity for the diffuse UGRB field is

$$G_\ell^\gamma(k) = \int \bar{\rho}_\gamma(z) b_\gamma(z) D(z) j_\ell[k\chi(z)] dz, \quad (5)$$

where $b_\gamma(z)$ is the linear bias of the γ-ray emitters, and $\bar{\rho}_\gamma(z)$ is their average flux density.

When the cross-correlation is computed for the whole catalog of sources, we consider the full dN/dz shown in Figure 2. When, instead, the cross-correlation is computed in a specific redshift bin, then we set the dN/dz equal to zero outside the redshift bin and equal to the original dN/dz inside the bin. The amplitude of the corresponding dN/dz is normalized to unity. For the distribution of the γ-ray emitters, $\bar{\rho}_\gamma(z)$, the situation is more complicated, since we do not observe $\bar{\rho}_\gamma(z)$ directly. In principle, the aim of the cross-correlation analysis is, indeed, to constrain this quantity, that is, to assume a model $\bar{\rho}_\gamma(z)$, predict the expected cross-correlation, and compare it with the observed one. This will be pursued in a follow-up analysis in which we shall consider physically motivated $\bar{\rho}_\gamma(z)$ models. Instead, here, where we aim for an illustrative, model-independent approach, we choose to have the average $\bar{\rho}_\gamma(z)$ in a given redshift bin as a free parameter. In this way, the absolute normalization of $\bar{\rho}_\gamma(z)$ is absorbed in the parameter A^{2h}. More precisely, when cross-correlating the UGRB with a catalog in a given redshift bin, the measured A^{2h} will be the product of three quantities. The first two are the average bias factors $b_c(z)$ and $b_\gamma(z)$ in the redshift range of the bin, and the third will be the average $\bar{\rho}_\gamma(z)$ in that bin.

We stress that this simple model tries to capture the angular correlation features of the expected cross-correlation signal without assuming any specific model for the sources of the UGRB. Its main goal is to separate the signal into 1-halo and 2-halo components and study their energy dependence. In a follow-up paper, we shall consider a physically motivated model, similar to that of Cuoco et al. (2015), including the contribution from all potential unresolved γ-ray sources

(blazars, misaligned AGNs, SFGs, decaying or annihilating nonbaryonic matter). Within this framework, it will be possible to explicitly specify the bias of the sources, their number density as a function of redshift, $\rho_\gamma(z)$, as well as their clustering.

Equation (2) models the CAPS for a single energy bin. However, since in this work we compute the cross-correlation signal in several energy bins, we can also use a CAPS model, which includes an explicit energy dependence. For this purpose, we have considered three different models specified below:

1. Single power law (SPL):

$$\hat{C}_\ell^{\gamma c}(E) = \Delta E (C^{1h} + A^{2h} C_\ell^{2h}) \cdot (E/E_0)^{-\alpha}, \quad (6)$$

where ΔE is the width of the energy bin considered in the cross-correlation analysis, α is the slope, and $E_0 = 1$ GeV is a normalization energy scale.

2. Double power law (DPL):

$$\hat{C}_\ell^{\gamma c}(E) = \Delta E \; C^{1h}(E/E_0)^{-\alpha_{1h}}$$
$$+ \Delta E \; A^{2h} C_\ell^{2h}(E/E_0)^{-\beta_{2h}}, \quad (7)$$

where the 1-halo and 2-halo terms are allowed to have two different power laws with slopes α and β.

3. Broken power law (BPL):

$$\hat{C}_\ell^{\gamma c}(E) = \Delta E (C^{1h} + A^{2h} C_\ell^{2h}) \cdot \begin{cases} (E/E_b)^{-\alpha}, & E > E_b \\ (E/E_b)^{-\beta}, & E < E_b \end{cases}, \quad (8)$$

characterized by a BPL with slopes α and β respectively above and below the break energy E_b.

To compare the data and models, we use standard χ^2 statistics for which we consider two implementations. When we focus on a single energy range and thus we ignore energy dependence, then we use

$$\chi^2 \equiv \chi^2(E, z, c) = \sum_{\ell \text{ bins}} \frac{(\hat{C}_\ell^{\gamma c} - C_\ell^{\gamma c})^2}{(\Delta C_\ell^{\gamma c})^2}, \quad (9)$$

where $\hat{C}_\ell^{\gamma c}$ and $C_\ell^{\gamma c}$ represent the model and the measured CAPS, the sum is over all ℓ bins, and the triplet (E, z, c) identifies the energy range, redshift bin, and object catalog considered in the analysis. The best-fitting C^{1h} and A^{2h} parameters are found by the minimization of the χ^2 function. Note that, in the following, together with C^{1h} we shall list the normalized value $A^{2h} C_{\ell=80}^{2h}$ that has the same dimension as C^{1h}. This choice is motivated by the fact that the fit constrains the product $A^{2h} C_\ell^{2h}$, rather than the single terms separately. The rationale for setting $\ell = 80$ is twofold. First of all, random errors are small at $\ell = 80$. Second, C_ℓ^{2h} peaks at $\ell \lesssim 100$ and then steadily declines and becomes subdominant with respect to the 1-halo term (see the relevant plots in X15 and Branchini et al. 2017). Considering $\ell \sim 80$ thus allows us to reasonably compare both the 1-halo and 2-halo terms. Note also that in the product $A^{2h} C_{\ell=80}^{2h}$ the second term is the *model* $C_{\ell=80}^{2h}$. As a result, the errors in $A^{2h} C_{\ell=80}^{2h}$ are propagated from the A^{2h} term only.

When we consider different energy bins and explicitly account for the CAPS energy dependence, then we use

$$\chi_e^2 \equiv \chi_e^2(z, c) = \sum_{\ell \text{ bins}} \sum_{E \text{ bins}} \frac{(\hat{C}_\ell^{\gamma c}(E_i) - C_\ell^{\gamma c}(E_i))^2}{(\Delta C_\ell^{\gamma c}(E_i))^2}, \quad (10)$$

where the sum is over both ℓ and energy bins, while the pair (z, c) identifies the redshift bin and object catalog considered in the analysis and the label e characterizes the model energy dependence of the CAPS, that is, $e =$ SPL, DPL, or BPL. In this case, the number of fitting parameters varies depending on e: three parameters for SPL, four for DPL, and five for BPL.

To quantify the significance of a measurement, we use as test statistic the quantity

$$\text{TS} = \chi^2(0) - \chi_{min}^2, \quad (11)$$

where χ_{min}^2 is the minimum χ^2, and $\chi^2(0)$ is the χ^2 of the null hypothesis, that is, of the case $C^{1h} = A^{2h} = 0$. TS is expected to behave asymptotically as a χ^2 distribution with a number of degrees of freedom equal to the number of fitted parameters, allowing us to derive the significance level of a measurement based on the measured TS.

Note that in Equation (2) $\hat{C}_\ell^{\gamma c}$, C^{1h}, and $A^{2h} C_\ell^{2h}$ all have units of $(\text{cm}^{-2} \text{ s}^{-1} \text{ sr}^{-1})$ sr, since they refer to CAPS of γ-ray flux maps integrated over the given energy bin. Instead, in Equations (6)–(8), C^{1h} and $A^{2h} C_\ell^{2h}$ have units of $(\text{cm}^{-2} \text{ s}^{-1} \text{ sr}^{-1} \text{ GeV}^{-1})$ sr, so $\hat{C}_\ell^{\gamma c}(E)$ still has units of $(\text{cm}^{-2} \text{ s}^{-1} \text{ sr}^{-1})$ sr. The results obtained in the two implementations described above, for the single and combined energy bins, are shown in Table 2 and in Table 3, respectively. Each sample in the tables is identified by the following label: CCCC ZX EY, where CCCC indicates the catalogs of extragalactic objects used in the cross-correlation (e.g., NVSS, 2MPZ), ZX identifies the redshift bin (e.g., Z1 for the first z bin, Z2 for the second, and ZA for the full redshift range), and EY identifies the energy bin (e.g., E1 for the first E bin, E2 for the second). In Table 2 we list the best-fit values of the parameters and their 1σ errors, whereas only the best-fit values are shown in Table 3. To perform the fit, we have assumed a frequentist approach. To derive the errors, we build for each parameter its 1D profile χ^2 minimizing the χ^2 with respect to the other parameters, and we calculate the 1σ errors from the condition $\Delta\chi^2 = 1$. In our analysis, we assume that CAPS is a positive quantity. Therefore, in the fit, we impose that both the 1-halo and 2-halo terms are nonnegative. For this reason, when 1σ is not limited from below, we just quote the 1σ upper limit.

In principle, cross-correlations can be negative. However, in our model, the cross-correlation between γ-ray sources and extragalactic objects is induced by the fact that both trace the same large-scale structure in some relatively compact redshift range. In this case, the CCF is not expected to be negative, motivating our constraint. Nonetheless, for the sake of completeness, we did perform the same fit after relaxing this constraint. We found that the 2-halo component can be negative when cross-correlating some catalogs with low (< 1 GeV) energy URGB maps. However, the preference for this fit over the nonnegative one is typically below 1σ and just in very few cases slightly above 1σ.

6. Results

In this section, we show the results of our cross-correlation analysis of the cleaned *Fermi*-LAT UGRB maps with the

Table 2
Best Fit to CAPS

Sample	$\chi^2_{\min}$	TS	σ	C_{1h}	$A_{2h}C_{80}$
NVSS ZA E1	20.3	15.0	3.5	47^{+12}_{-13}	<15.7
NVSS ZA E2	32.7	110	10.3	$26.1^{+2.6}_{-2.7}$	<4.95
NVSS ZA E3	5.49	64.4	7.7	$0.94^{+0.12}_{-0.11}$	<0.372
QSO ZA E1	5.53	7.25	2.2	<29.9	<23.8
QSO ZA E2	11.3	12.0	3.0	$5.7^{+1.7}_{-2.1}$	<5.18
QSO ZA E3	11.4	12.3	3.1	<0.22	$0.71^{+0.26}_{-0.288}$
2MPZ Z1 E1	4.40	0.20	0.1	<90.7	<59.8
2MPZ Z1 E2	7.97	4.27	1.6	<24.9	<24.8
2MPZ Z1 E3	15.5	4.04	1.5	<0.780	<1.79
2MPZ Z2 E1	8.64	0.168	0.1	<62.7	<49.7
2MPZ Z2 E2	6.35	1.11	0.6	<12.5	<21.7
2MPZ Z2 E3	9.33	3.25	1.3	<0.448	<2.15
2MPZ Z3 E1	6.89	1.88	0.9	<94.9	<47.5
2MPZ Z3 E2	2.44	15.4	3.5	$19.8^{+5.1}_{-7.0}$	<20.7
2MPZ Z3 E3	8.26	17.1	3.7	$0.71^{+0.21}_{-0.23}$	<2.15
2MPZ ZA E1	7.85	0.911	0.5	<59.8	<37.7
2MPZ ZA E2	8.18	8.18	2.4	$8.6^{+3.5}_{-4.3}$	<18.7
2MPZ ZA E3	12.3	13.3	3.2	$0.31^{+0.11}_{-0.13}$	<1.63
WIxSC ZA E1	16.2	22.0	4.3	$32.8^{+7.3}_{-7.0}$	<5.95
WIxSC ZA E2	9.32	26.5	4.8	$4.1^{+1.5}_{-1.7}$	<11.4
WIxSC ZA E3	1.99	35.3	5.6	$0.098^{+0.040}_{-0.040}$	$0.56^{+0.26}_{-0.27}$
MG12 ZA E1	6.90	11.5	2.9	$21.7^{+9.8}_{-10.8}$	<31.4
MG12 ZA E2	7.69	26.9	4.8	$3.0^{+1.6}_{-1.5}$	$6.8^{+3.4}_{-3.3}$
MG12 ZA E3	8.73	23.5	4.5	$0.098^{+0.032}_{-0.034}$	<0.780

Note. Column 1: subsample name. Column 2: minimum χ^2 value. Columns 3 and 4: values of the test statistic TS $= \chi^2(0) - \chi^2_{\min}$ and corresponding statistical significance. Columns 5 and 6: 68% C.L. constraints on the 1-halo term C_{1h} and on the 2-halo term $A_{2h} \times C_{\ell=80}$, both expressed in units of 10^{13} (cm^{-2} s^{-1} sr^{-1}) sr. The fit in each row is performed using 12 data points and two fit parameters, for a total of 10 degrees of freedom.

Table 3
CAPS Energy Dependence

Sample	$\chi^2_{\min}$	TS	σ	α_{1h}	β_{2h}	C_{1h}	$A_{2h}C_{80}$
NVSS ZA	126.	274.0	16.1	2.32	4.54	44.1	0.0466
QSO6 Z1	108.	18.0	3.2	3.59	1.50	17.0	0.769
QSO6 Z2	96.0	5.14	1.1	3.30	2.17	5.72	2.62
QSO6 Z3	94.3	20.5	3.5	3.19	2.05	8.31	11.8
WIxSC Z1	93.7	19.8	3.5	2.48	1.58	11.3	0.0357
WIxSC Z2	96.3	25.7	4.1	2.39	1.80	5.39	1.85
WIxSC Z3	71.4	62.9	7.2	2.30	1.87	7.00	3.60
WIxSC Z4	82.2	34.1	5.0	1.90	2.67	1.29	23.6
2MPZ Z1	83.7	8.1	1.7	2.53	3.53	21.7	0.0328
2MPZ Z2	61.7	6.58	1.4	1.89	2.51	1.76	8.45
2MPZ Z3	69.6	38.3	5.3	2.22	1.77	22.8	1.35
MG12 Z1	56.4	13.9	2.7	2.03	1.91	3.11	2.05
MG12 Z2	82.1	19.2	3.4	4.47	2.02	2.97	12.3
MG12 Z3	86.4	46.7	6.0	2.23	2.00	3.86	10.3
MG12 Z4	69.4	42.4	5.7	3.59	1.95	16.2	8.23
MG12 Z5	80.5	41.4	5.6	3.79	2.07	14.1	9.99
MG12 Z6	61.4	27.1	4.3	2.36	2.38	6.22	11.2
MG12 Z7	69.7	12.4	2.5	2.28	2.34	6.64	2.44

Note. Results of the best fit when the double power law model is assumed. Column 1: subsample considered. Column 2: minimum χ^2 value (the χ^2 is calculated as a sum over eight energy bins and 12 multipole bins, i.e., 96 bins in total, and the number of fitted parameters is four, for a total of 92 degrees of freedom). Columns 3 and 4: values of the test statistic TS $= \chi^2(0) - \chi^2_{\min}$ and corresponding statistical significance. Columns 5 and 6: best-fit slopes of the 1-halo and 2-halo power-law energy dependence. Columns 7 and 8: best-fit values of the 1-halo term C_{1h} and 2-halo term $A_{2h} \times C_{\ell=80}$, both expressed in units of $10^{13} \times$ (cm^{-2} s^{-1} sr^{-1} GeV^{-1}) sr.

angular distributions of objects in the various catalogs presented in Section 3. As already mentioned, we shall plot the CCFs, whose visual interpretation in the framework of the halo model is more transparent. However, the statistical analyses and the results listed in the tables are obtained from the measured CAPS, after deconvolution from pixel and PSF effects.

For each catalog we show three sets of results. The first one includes the results of the CAPS χ^2 analysis (Equation (9)) restricted to well-defined, relatively wide energy bins $E = [0.5, 1]$ GeV, $E = [1, 10]$ GeV, and $E = [10, 500]$ GeV. The results of this analysis are listed in Tables 2 and 4. The first one contains the results of the plots that are shown in the main text. This subset includes all analyses of the full sample catalogs (ZA case) and, for the 2MPZ case only, also the analyses of the individual redshift bins. The latter serve to illustrate the advantage of performing a tomographic approach with respect to that of considering the full redshift range, as X15 did using the whole 2MASS sample. The second table, located in Appendix B, contains all results from the subsamples considered in the analysis. The corresponding plots are also shown in the same appendix.

The second set of results is similar to the first one, but we consider eight narrow energy bins instead of the three wide ones. In this case, we do not quote results of the fit in a table, but display them in plots in which we show the best-fit 1-halo and 2-halo terms as well as their sum as a function of energy. As a general remark, we note that errors on the 1-halo and 2-halo terms measured in the narrow energy bins are large, often resulting only in upper limits. This is because the two terms are typically not clearly separable given the large CAPS error bars. For this reason, in the plots we shall show also the sum of the two, which is more tightly constrained and thus has smaller errors.

The results of the CAPS energy-dependent fit are part of the third set of results. In this case we considered three models: SPL, DPL, and BPL (Equations (6)–(8)). The statistical significance of the results is similar in the three cases, so the SPL model is satisfactory. Nonetheless, since in a few cases the DPL gives a slightly better fit (in particular, for the MG12 Z4, Z5 cases, which both have $\Delta\chi^2 = \chi^2_{SPL} - \chi^2_{DPL} \approx 6$ corresponding to ~2.4σ improvement), we decided to focus mainly on this latter model, whose results are reported in Table 3, while results for all three models are listed in Appendix B. We will show in each plot the best-fit DPL model, together with the 1-halo and 2-halo terms and their errors derived from the fit in each narrow energy bin separately. Note that, for better clarity of the plots, we will show only the best-fit model, and we will omit the associated error band, which is typically quite large, especially for the 1-halo and 2-halo component singularly. We

Table 4
Best Fit to CAPS

Sample	$\chi^2_{\min}$	TS	σ	C_{1h}	$A_{2h}C_{80}$	Sample	$\chi^2_{\min}$	TS	σ	C_{1h}	$A_{2h}C_{80}$
NVSS ZA E1	20.3	15.0	3.5	47^{+12}_{-13}	<15.7	2MPZ Z1 E1	4.40	0.20	0.1	<90.7	<59.8
NVSS ZA E2	32.7	110	10.3	$26.1^{+2.6}_{-2.7}$	<4.95	2MPZ Z1 E2	7.97	4.27	1.6	<24.9	<24.8
NVSS ZA E3	5.49	64.4	7.7	$0.94^{+0.12}_{-0.11}$	<0.372	2MPZ Z1 E3	15.5	4.04	1.5	<0.780	<1.79
QSO Z1 E1	10.4	11.9	3.0	41^{+12}_{-21}	<26.1	2MPZ Z2 E1	8.64	0.168	0.1	<62.7	<49.7
QSO Z1 E2	10.8	1.21	0.6	<9.89	<6.83	2MPZ Z2 E2	6.35	1.11	0.6	<12.5	<21.7
QSO Z1 E3	10.3	6.11	2.0	<0.470	<1.56	2MPZ Z2 E3	9.33	3.25	1.3	<0.448	<2.15
QSO Z2 E1	9.47	0.897	0.5	<24.9	<26.1	2MPZ Z3 E1	6.89	1.88	0.9	<94.9	<47.5
QSO Z2 E2	14.1	3.42	1.3	<9.01	<10.4	2MPZ Z3 E2	2.44	15.4	3.5	$19.8^{+5.1}_{-7.0}$	<20.7
QSO Z2 E3	5.00	3.22	1.3	<0.258	<1.24	2MPZ Z3 E3	8.26	17.1	3.7	$0.71^{+0.21}_{-0.23}$	<2.15
QSO Z3 E1	13.9	1.35	0.7	<36.0	<41.4	2MPZ ZA E1	7.85	0.911	0.5	<59.8	<37.7
QSO Z3 E2	8.60	11.9	3.0	<17.2	<20.7	2MPZ ZA E2	8.18	8.18	2.4	$8.61^{+3.54}_{-4.30}$	<18.7
QSO Z3 E3	10.7	7.93	2.3	<0.310	$1.08^{+0.36}_{-0.47}$	2MPZ ZA E3	12.3	13.3	3.2	$0.31^{+0.11}_{-0.13}$	<1.63
QSO ZA E1	5.53	7.25	2.2	<29.9	<23.8	MG12 Z1 E1	7.70	1.40	0.7	<34.4	<24.9
QSO ZA E2	11.3	12.0	3.0	$5.7^{+1.7}_{-2.1}$	<5.18	MG12 Z1 E2	9.60	1.76	0.8	<10.4	<16.4
QSO ZA E3	11.4	12.3	3.1	<0.224	$0.71^{+0.26}_{-0.29}$	MG12 Z1 E3	4.32	6.16	2.0	<0.356	<1.79
WIxSC Z1 E1	14.8	3.56	1.4	<52.1	<23.8	MG12 Z2 E1	5.29	3.20	1.3	<45.4	<27.3
WIxSC Z1 E2	16.0	8.50	2.4	$6.2^{+2.1}_{-2.4}$	<7.85	MG12 Z2 E2	8.24	5.55	1.9	<5.18	<17.2
WIxSC Z1 E3	16.0	5.55	1.9	<0.258	<1.36	MG12 Z2 E3	7.79	7.41	2.2	<0.178	<1.42
WIxSC Z2 E1	11.7	4.17	1.5	<39.5	<13.0	MG12 Z3 E1	9.35	5.95	2.0	<47.5	<21.7
WIxSC Z2 E2	3.67	9.73	2.7	$4.3^{+1.6}_{-2.1}$	<9.01	MG12 Z3 E2	5.74	13.3	3.2	$4.1^{+2.4}_{-2.1}$	<16.4
WIxSC Z2 E3	12.4	15.6	3.5	<0.141	$0.71^{+0.29}_{-0.32}$	MG12 Z3 E3	14.0	19.1	4.0	$0.10^{+0.061}_{-0.051}$	$0.78^{+0.43}_{-0.39}$
WIxSC Z3 E1	12.9	7.52	2.3	$24.9^{+9.2}_{-9.8}$	<15.7	MG12 Z4 E1	7.04	4.93	1.7	<37.7	<31.4
WIxSC Z3 E2	4.54	16.2	3.6	$4.7^{+1.6}_{-1.9}$	<10.4	MG12 Z4 E2	5.52	17.5	3.8	$4.3^{+2.0}_{-2.0}$	<14.3
WIxSC Z3 E3	5.39	22.4	4.3	$0.178^{+0.034}_{-0.050}$	<0.619	MG12 Z4 E3	5.00	7.86	2.3	<0.170	<0.896
WIxSC Z4 E1	9.94	7.98	2.4	<24.9	33^{+12}_{-15}	MG12 Z5 E1	8.12	11.0	2.9	<43.3	<37.7
WIxSC Z4 E2	12.0	9.92	2.7	<5.95	$10.4^{+3.8}_{-5.2}$	MG12 Z5 E2	5.73	12.9	3.2	<6.83	<15.0
WIxSC Z4 E3	9.67	8.02	2.4	$0.155^{+0.064}_{-0.072}$	<0.896	MG12 Z5 E3	10.3	5.33	1.8	<0.162	<0.711
WIxSC ZA E1	16.2	22.0	4.3	$32.8^{+7.3}_{-7.0}$	<5.95	MG12 Z6 E1	6.67	7.54	2.3	<49.7	<41.4
WIxSC ZA E2	9.32	26.5	4.8	$4.1^{+1.5}_{-1.7}$	<11.4	MG12 Z6 E2	6.93	15.5	3.5	<9.89	<19.8
WIxSC ZA E3	1.99	35.3	5.6	$0.098^{+0.040}_{-0.040}$	$0.56^{+0.26}_{-0.27}$	MG12 Z6 E3	13.7	7.00	2.2	$0.155^{+0.057}_{-0.065}$	<0.711
						MG12 Z7 E1	7.62	1.08	0.6	<24.9	<29.9
						MG12 Z7 E2	3.94	6.21	2.0	<11.4	<9.44
						MG12 Z7 E3	13.9	4.80	1.7	<0.390	<0.515
						MG12 ZA E1	6.90	11.5	2.9	$21.7^{+9.8}_{-10.8}$	<31.4
						MG12 ZA E2	7.69	26.9	4.8	$3.0^{+1.6}_{-1.5}$	$6.8^{+3.4}_{-3.3}$
						MG12 ZA E3	8.73	23.5	4.5	$0.098^{+0.032}_{-0.034}$	<0.780

Note. Column 1: subsample name. Column 2(7): minimum χ^2 value. Columns 3(8) and 4(9): values of the test statistics TS $= (\chi^2(0) - \chi^2_{\min})$ and corresponding statistical significance. Columns 5(10) and 6(11): 68% C.L. constraints on the 1-halo term C_{1h} and on the 2-halo term $A_{2h} \times C_{\ell=80}$, both expressed in units of $10^{13} \times (\text{cm}^{-2}\,\text{s}^{-1}\,\text{sr}^{-1})$ sr. The fit in each row is performed using 12 data points and two fit parameters, for a total of 10 degrees of freedom.

will, in the following, use this best-fit model to make some qualitative comment on the preferred energy spectrum of the correlation and its eventual evolution in redshift, or differences between the catalogs.

6.1. Cross-correlation with NVSS Galaxies

The results of this analysis can be directly compared with those of X15 to assess the improvement obtained by using the P8 LAT data. In this case, no tomographic analysis is performed here since redshift measurements are not available for the majority of the NVSS objects.

The left panel of Figure 7 shows the CCFs measured in three energy bins: [0.5, 1], [1, 10], and [10, 500] GeV. The corresponding CAPS data are also shown in the right panel for reference. A significant, positive correlation signal is detected for $\theta < 1°$ at all energies, with a statistical significance of, respectively, 3.5, 10.3, and 7.7σ in the three energy bins. The corresponding best-fitting 1- and 2-halo terms are listed in Table 2. This result is similar to that of X15, indicating that, for the NVSS case, errors are dominated by systematic effects. In the lowest energy bin, the significance has decreased (9.9 to 3.5σ). This apparent inconsistency derives from the fact
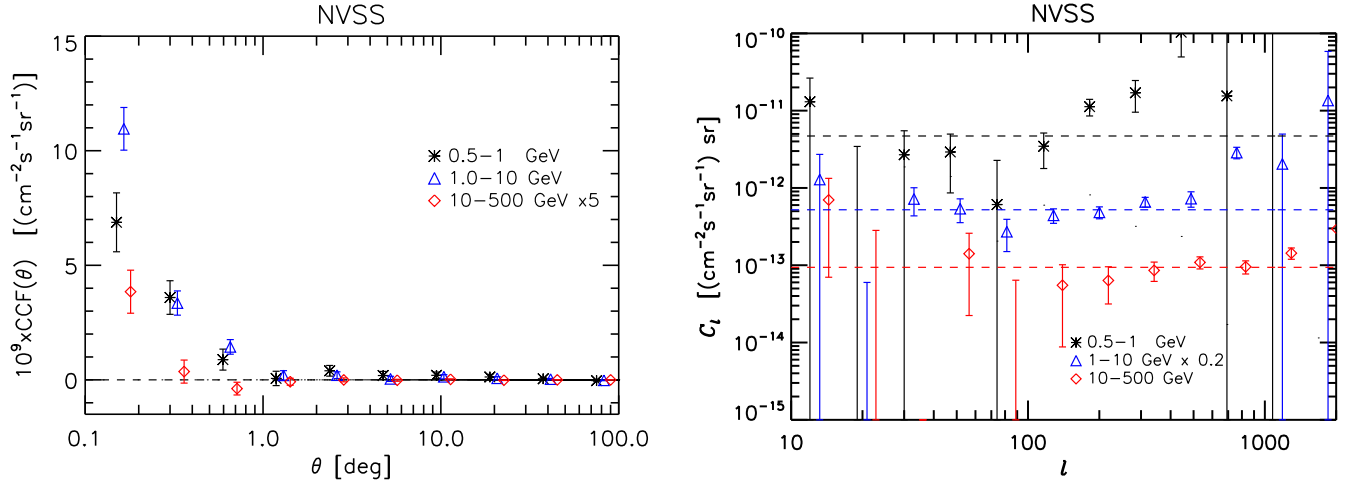
Figure 7. Angular CCF (left) and CAPS (right) for NVSS galaxies. Different symbols indicate the three energy bins: [0.5, 1], [1, 10], and [10, 500] GeV. Error bars represent the square root of the diagonal elements of the covariance matrix (which, for the CAPS, is to a good approximation diagonal). Furthermore, the CAPS data have been deconvolved by the PSF and pixel effects. Dashed lines in the right-hand plot show the best-fit values of the 1-halo term C_{1h} from Table 2.

that X15 considered all photons with $E > 0.5$ GeV, while we consider only those with $0.5 < E < 1$ GeV.

As in X15, the CCF signal is quite localized. It is strongly dominated by the 1-halo term, and the contribution of the 2-halo term is negligible. The χ^2 analysis of the CAPS confirms this impression. Table 2 shows that the cross-correlation signal is indeed dominated by the term C_{1h}, which is clearly detected in all energy bins, whereas for the 2-halo term, $A_{2h}C_{80}$, we obtain only upper limits. In the right-hand panel of Figure 7, the best-fit values of C_{1h} are shown together with the PSF-deconvolved CAPS. The energy dependence of the best-fitting 1- and 2-halo terms in the eight narrow energy bins is presented in Figure 8. The 1-halo term dominates over a large fraction of the energy range considered. The contribution from the 2-halo term becomes significant beyond 30 GeV and matches the 1-halo term at $\sim$100 GeV.

Based on this evidence, we confirm the interpretation proposed by X15: the cross-correlation signal arises from NVSS objects also emitting in γ-rays. This is a sound argument since radio galaxies are often associated with γ-ray emitters (Acero et al. 2015). However, this interpretation does not hold at very high energies. At $E \sim 100$ GeV, the cross-correlation has a significant 2-halo component, and it is thus contributed by γ-ray sources residing in different halos than those of the nearest NVSS source. From Table 3, for the DPL model, the slope of the 1-halo term is $\sim$2.3, while the 2-halo component is basically rejected by the fit and in the plot is seen to give some contribution only at very low energies. In particular, at $\sim$100 GeV, the DPL fit predicts a 2-halo term that is several orders of magnitude smaller than the 2-halo data point inferred from a fit performed using eight narrow energy bins. This mismatch appears either because the DPL fit is dominated by the low-energy data points, where indeed the 1-halo term dominates, or because a simple power law is not able to represent well the 2-halo component at $\sim$100 GeV without overpredicting the amplitude of the 2-halo term at lower energies. The global significance of the NVSS signal in terms of the DPL (with four free parameters) is 16.1σ. Adding more parameters using the BPL model does not improve the fit significantly (see Table 5).
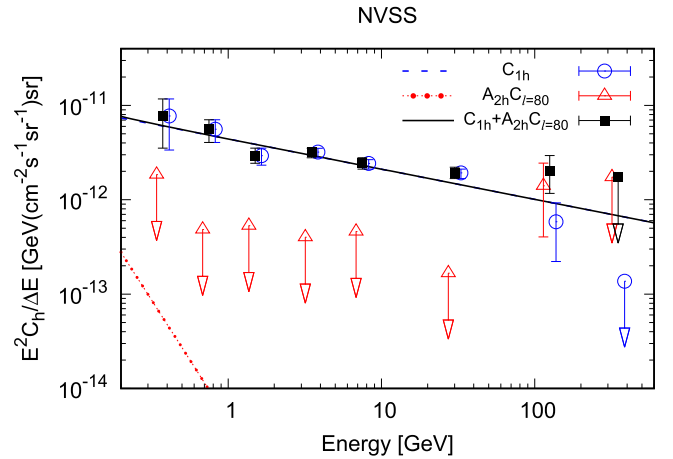
Figure 8. Energy dependence of the C_{1h} and $A_{2h}C_{80}$ terms and of their sum. The symbols represent the best-fit values in each energy bin. Bars represent 1σ errors. In the case of upper limits, a downward arrow is shown. The plot also shows the best-fit DPL model (black solid line), as well as the 1-halo (blue dashed) and 2-halo (red dotted) components. Their numerical values are listed in Table 3. Note that in this case the blue line is not visible, since it overlaps completely with the black one.

6.2. Cross-correlation with SDSS DR6 QSO

Figure 9 is analogous to Figure 7 and shows the CCFs of P8 LAT data with the full SDSS DR6 QSO sample, covering the whole redshift range $z \in [0, 4]$, in three energy bins. The result is directly comparable with the one of X15, where the same quasar sample was used. A positive cross-correlation is detected out to $\theta \sim 1°$, with a significance of 2.2σ in the low-energy bin and $\sim 3\sigma$ in the two high-energy ones (see Table 2).

The availability of photometric redshifts for this QSO sample allows us to decompose the signal tomographically, which provides insight into the possible evolution of the γ-ray sources associated with the quasar distribution. The results are shown in Figure 10. Contrary to the NVSS case, the 2-halo term is now prominent except for, perhaps, at low energies and low redshifts. The plots also show an evolution of the

Table 5
CAPS Energy Dependence

Sample	χ^2_{min}	TS	σ	α	C_{1h}	$A_{2h}C_{80}$	χ^2_{min}	TS	σ	α_{1h}	β_{2h}	C_{1h}	$A_{2h}C_{80}$	χ^2_{min}	TS	σ	E_{break}	α	β	C_{1h}	$A_{2h}C_{80}$
			SPL							DPL							BPL				
NVSS ZA	126.	274.0	16.2	2.32	44.5	0.035	126.	274.0	16.1	2.32	4.54	44.1	0.047	118.	282.0	16.2	2.33	2.27	8.32	41.9	0.005
QSO6 Z1	110.	16.0	3.3	3.25	19.8	0.055	108.	18.0	3.2	3.59	1.50	17.0	0.769	107.	19.0	3.1	1.40	3.27	2.52	20.0	0.742
QSO6 Z2	96.1	5.04	1.4	3.07	8.13	0.573	96.0	5.14	1.1	3.30	2.17	5.72	2.62	95.7	5.44	0.9	0.939	8.05	3.11	96.2	20.4
QSO6 Z3	95.6	19.2	3.7	2.19	0.033	18.2	94.3	20.5	3.5	3.19	2.05	8.31	11.8	94.0	20.8	3.3	1.22	2.37	2.17	0.088	23.6
WIxSC Z1	93.8	19.8	3.7	2.41	10.4	0.0071	93.7	19.9	3.5	2.48	1.58	11.3	0.036	93.5	20.1	3.2	2.03	2.35	2.81	9.40	0.295
WIxSC Z2	96.7	25.3	4.3	2.18	3.26	3.97	96.3	25.7	4.1	2.39	1.80	5.39	1.85	93.5	28.5	4.2	1.08	3.17	2.51	15.1	0.457
WIxSC Z3	71.6	62.7	7.3	2.21	5.65	6.22	71.4	62.9	7.2	2.30	1.87	7.00	3.60	70.5	63.9	7.1	1.25	2.56	2.35	10.6	4.14
WIxSC Z4	85.7	30.6	4.9	2.24	2.79	16.8	82.2	34.1	5.0	1.90	2.67	1.29	23.6	83.2	33.2	4.6	1.40	2.65	2.27	5.41	21.1
2MPZ Z1	83.8	7.98	2.0	2.50	22.5	0.486	83.7	8.1	1.7	2.53	3.53	21.7	0.033	81.7	10.1	1.8	1.72	2.12	8.82	10.7	0.798
2MPZ Z2	62.6	5.68	1.6	2.00	2.58	4.54	61.7	6.58	1.4	1.89	2.51	1.76	8.45	62.4	5.88	1.0	0.576	5.21	2.35	10.7	16.3
2MPZ Z3	69.7	38.2	5.5	2.22	24.0	0.173	69.6	38.3	5.3	2.22	1.77	22.8	1.35	66.5	41.4	5.4	1.03	2.53	2.28	33.6	2.51
MG12 Z1	56.5	13.8	3.0	2.03	3.16	2.97	56.4	13.9	2.7	2.03	1.91	3.11	2.05	55.3	15.0	2.6	0.461	7.43	2.06	3.08	8.95
MG12 Z2	83.0	18.3	3.5	2.06	0.084	13.4	82.1	19.2	3.4	4.47	2.02	2.97	12.3	82.8	18.5	3.0	1.34	2.17	2.03	0.0690	14.5
MG12 Z3	86.7	46.4	6.2	2.13	3.18	12.5	86.4	46.7	6.0	2.23	2.00	3.86	10.3	85.4	47.7	5.9	1.07	2.44	2.19	4.85	12.3
MG12 Z4	75.5	36.3	5.4	2.32	2.15	19.2	69.4	42.4	5.7	3.59	1.95	16.2	8.23	73.3	38.5	5.1	1.41	3.02	2.50	9.38	18.2
MG12 Z5	86.7	35.2	5.4	2.64	4.05	22.7	80.5	41.4	5.6	3.79	2.07	14.1	9.99	83.7	38.2	5.1	1.36	2.96	2.53	7.57	17.2
MG12 Z6	61.5	27.0	4.5	2.30	5.45	11.4	61.4	27.1	4.3	2.36	2.38	6.22	11.2	61.0	27.5	4.1	0.902	2.55	2.35	7.07	10.8
MG12 Z7	69.8	12.3	2.7	2.30	7.27	2.89	69.7	12.4	2.5	2.28	2.34	6.64	2.44	68.7	13.4	2.3	2.30	2.39	2.19	8.80	1.14

Note. Results of the best fit when the SPL, DPL, and BPL models are used. Column 1: subsample considered. Columns 2, 7, and 12: minimum χ^2 values (the χ^2 is calculated as a sum over eight energy bins and 12 multipole bins, i.e., 96 bins in total, and the number of fitted parameters is three for the SPL fit, four for the DPL fit, and five for the BPL fit, for a total of 93, 92, and 91 degrees of freedom, respectively). Columns 3, 8, and 13 and 4, 9, and 14: values of the test statistics $TS = (\chi^2(0) - \chi^2_{min})$ and corresponding statistical significance. Columns 5, 10, and 15 and 6, 11, and 16: best-fit values of the 1-halo term C_{1h} and 2-halo term $A_{2h} \times C_{\ell=80}$, both expressed in units of $10^{13} \times$ (cm^{-2} s^{-1} sr^{-1} GeV^{-1}) sr.
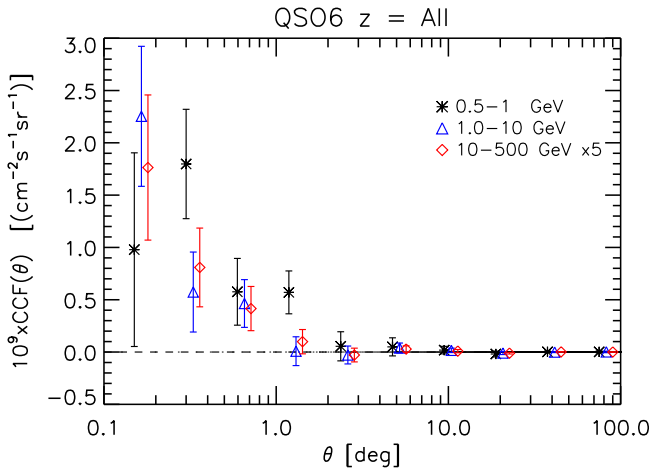
Figure 9. Same as the left panel of Figure 7 but for the cross-correlation of the full SDSS DR6 QSO sample with *Fermi*-LAT P8 data.

correlation signal as a function of redshift, suggesting that the UGRB is contributed by different sources at different redshifts. In particular, at $z < 1$, the CAPS energy spectrum has a two-component structure with a steep 1-halo term below $E \simeq 10$ GeV and a harder 2-halo term above it. Instead, at larger redshifts, the 2-halo term is prominent at all energies with a flat spectrum with slope ~ 2.

6.3. Cross-correlation with 2MPZ Galaxies

This catalog supersedes and largely overlaps with the 2MASS one used by X15. The availability of photo-z's for all 2MPZ objects allows us to slice up the sample and carry out a tomographic study in three independent redshift bins out to $z = 0.4$ (although we note that there are practically no 2MPZ galaxies beyond $z \sim 0.3$; see Figure 2).

The CCFs of 2MPZ galaxies and *Fermi*-LAT P8 maps are shown in Figure 11, for the full sample and for the three redshift shells $z \in [0, 0.06]$, [0.06, 0.12], and [0.12, 0.4]. Unlike the other catalogs, we show in the main text the CCFs also for the redshifts bins, to discuss more in detail the comparison with the results of X15 and to illustrate the importance of performing tomographic studies.

For the full sample case (top left panel of Figure 11), the results are directly comparable with X15. From Table 2 we see that the statistical significance in the second energy bin is similar to the one found in X15, while for the third bin ($E > 10$ GeV) the significance has increased noticeably thanks to the larger statistics. Again, as for NVSS and SDSS QSOs, the significance in the first energy bin is smaller than the one reported in X15, which is attributable to the different energy ranges of the bins. This also means that the correlation seen in X15 for the energy range $E > 0.5$ GeV had, apparently, a significant contribution from the γ-ray events with $E > 1$ GeV.

Figure 11 and Tables 2 and 3 all show little or no correlation in the first two redshift bins of 2MPZ. The CCF signal is instead largely generated in the third redshift bin, at $z > 0.12$. This is quite unexpected since in this redshift range we sample the tail of the 2MPZ distribution (see Figure 2), whereas a large fraction of 2MPZ galaxies populate the second z bin, where the peak is located.

This puzzling result suggests that the nature of 2MPZ objects changes at these redshifts, which is consistent with the fact that the bias of these sources also increases significantly from $b \sim 1$ to $b \sim 2$ (Francis & Peacock 2010; Steward 2014). This reflects, at least in part, the flux-limited nature of the sample. 2MPZ galaxies at higher redshifts are intrinsically brighter and trace the peaks of the underlying density field, which results in a larger autocorrelation signal and, thus, a larger b.

The result that γ-rays preferentially correlate with high-z 2MPZ galaxies rather than with the low-z ones illustrates explicitly the added value of the tomographic approach. It also shows that an analysis based on the full sample, like in X15, can lead to partial, if not biased, conclusions. The other advantage of the tomographic approach is that the above result can be cross-checked using other catalogs and selecting objects in the same redshift interval. We will, indeed, discuss this comparison in the next sections in relation to WI×SC and SDSS DR12.

Comparing the CCF of the full 2MPZ z range (Figure 11) with the one of 2MASS from X15, a factor of ~ 2 mismatch in the normalization is visible. After cross-checks, we found the origin of this inconsistency. It was due to an error in the derivation of the exposure map in each energy bin, which led in X15 to an incorrect normalization of the flux maps and thus of the derived CCF and CAPS. The results of the present analysis thus supersede the ones in X15 not only because of the better statistics and the tomographic approach, but also because of the updated normalization. We stress, nonetheless, that the results obtained from the analysis of X15 (e.g., Cuoco et al. 2015 and Regis et al. 2015) are generally valid except for the fact that the estimated quantities should be rescaled by a factor of ~ 2.

The plots in Figure 12 show the energy dependence of the correlation signal. Again, it can be seen that the signal is quite weak in the first two z bins and stronger in the third one. In this bin, the signal is compatible with a flat energy spectrum and shows a preference for a 1-halo term, although a nonnegligible 2-halo contribution is also present.

6.4. Cross-correlation with WISE× SuperCOSMOS Galaxies

The cross-correlation of the UGRB with WI×SC is performed here for the first time. The WI×SC catalog contains many more galaxies than the 2MPZ one, although its photometric redshifts are measured less precisely. However, thanks to the larger depth of WI×SC, we are able to perform a similar tomographic analysis using four thicker and not overlapping redshift slices.

As for all the other catalogs but the 2MPZ one, in the main text we only show the result for the full z range (Figure 13). The CCFs for the individual redshift shells are shown in Appendix B. The energy dependence of the correlation in the various redshift shells is shown in Figure 14. A 1-halo component is favored for $z < 0.3$, although a 2-halo contribution is allowed within the uncertainties, except perhaps at energies <1 GeV and $z < 0.09$. In the range $z \in [0.3, 0.5]$, instead, the 2-halo component is favored at all energies. A redshift evolution of the energy spectrum is also evident. The spectrum is close to flat for $z \in [0.09, 0.3]$ and much steeper with a prominent low-energy tail for $z \in [0.3, 0.5]$. This, again, confirms the importance of splitting the analysis into redshift shells. The statistical significance of the signal is above 3.7σ in all z bins, reaching 7.2σ for
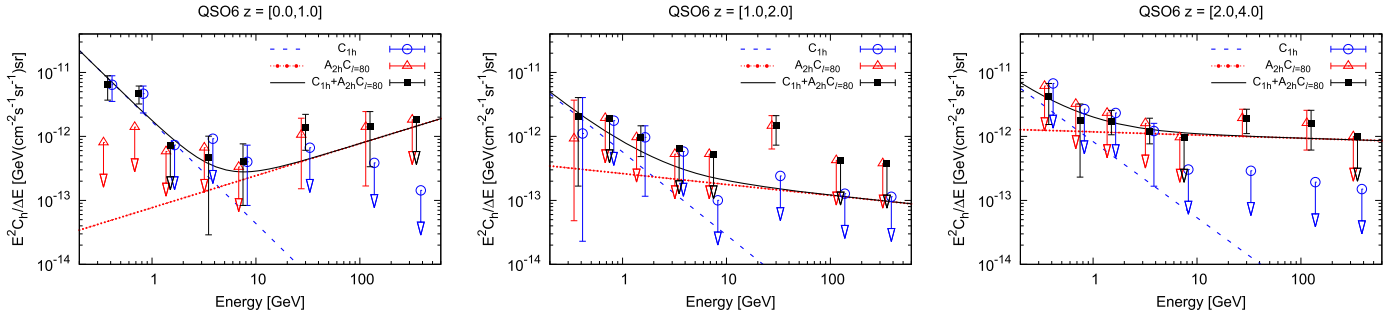
Figure 10. Same as Figure 8 but for the DR6 QSO CAPS measured in three redshift bins: $z \in [0.0, 1.0]$ (left), $z \in [1.0, 2.0]$ (middle), $z \in [2.0, 4.0]$ (right).
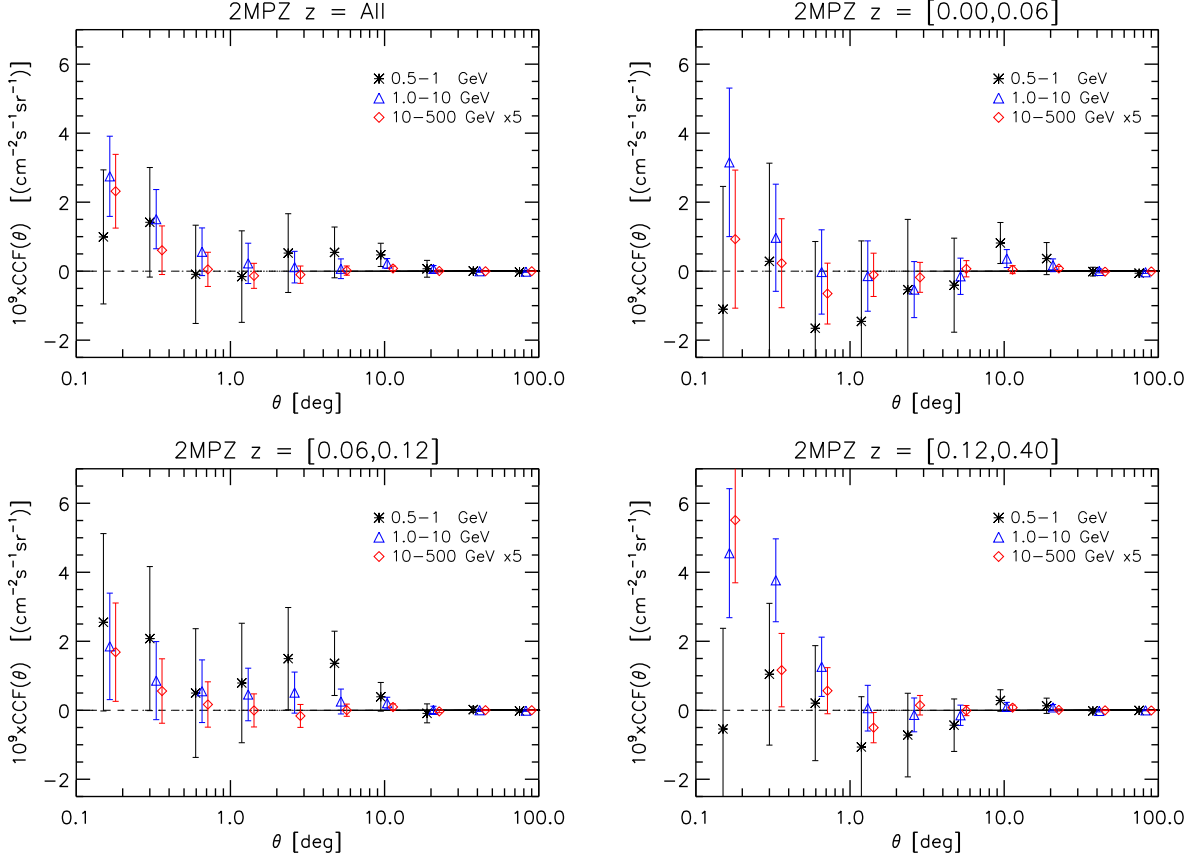

Figure 11. Same as the left panel of Figure 7 but for the cross-correlation of the full 2MPZ sample with *Fermi*-LAT P8 data, as well as for the three redshift slices adopted in the analysis.

$z \in [0.21, 0.3]$ (Table 3). Combining the significances from all of the z bins gives a global significance for the WI×SC signal of $\sqrt{\sum_i \sigma_i^2} \approx 10.4\sigma$.

6.5. Cross-correlation with SDSS DR12 Photometric Galaxies

X15 cross-correlated the SDSS DR8 data sets with 60-month *Fermi*-LAT data. Here we update that analysis using the *Fermi*-LAT P8 maps and the SDSS DR12 photometric catalog sliced up into seven redshift bins.

The CCF obtained by considering the catalog of all objects (reaching out to $z = 1.0$) is shown in Figure 15. A cross-correlation signal is detected within 1° in all energy bands, with a significance of about 3.0, 4.7, and 4.5σ, respectively (see

Table 2), which corresponds to a global significance of about $\sqrt{\sum_i \sigma_i^2} \approx 7\sigma$. Much more information can, however, be extracted from the tomographic analysis.

The CCFs measured in the seven z bins are shown in Appendix B, while their corresponding energy spectra are shown in Figure 16. The amplitude and the nature of the cross-correlation signal varies significantly with redshift. One remarkable feature is that at high energy ($E > 10$ GeV) the signal is quite local, with an amplitude that is largest at $z \sim 0.3$ and negligible at higher redshifts. A second characteristic is the bimodal nature of the signal. The 2-halo component typically dominates above ~ 5 GeV at all redshifts, whereas the 1-halo term, characterized by a steeper spectrum, is more important

below ∼5 GeV. This suggests that SDSS galaxies trace two different populations of γ-ray emitters. The first one is made of relatively low energy γ-ray sources, with a steep spectrum (slope of ∼2.3 or larger, from Table 3), that typically reside in the same DM halos as the SDSS galaxies. The second population is composed of high-energy sources typically located in a different halo and with a flat (slope ∼2, see again Table 3) energy spectrum.

The energy spectrum also shows an interesting feature in the form of a bump at about ∼10 GeV in the redshift range $z \in [0.3, 0.4]$. Such a feature is also seen in the WI×SC correlation at $z \in [0.3, 0.5]$. The bump is seen in the 2-halo term only. Moreover, the bump seems to be present, although less prominently, also at $z \in [0.4, 0.5]$ and at $z \in [0.5, 0.6]$, but at energies slightly below 10 GeV, as could be expected from a cosmologically redshifted signal, further suggesting that the bump may be a real feature instead of a statistical fluctuation. If this is indeed the case, then it would be difficult to justify the bump using conventional astrophysical processes. The tantalizing hypothesis of an exotic process, like that of DM annihilation, could be then advocated. We do not attempt here to quantify the statistical significance of this feature. We postpone its quantitative analysis and interpretation to a future work in which exotic sources will be included among more conventional γ-ray source populations.

Table 3 shows that the significance of the cross-correlation signal ranges from 2.5σ, in the highest z bin, to 6σ, in the third z bin. The difference with the unbinned case is striking: the statistical significance of the CCF signal measured in the full z bin is 7σ, while the one obtained from the tomographic analysis is $\sim \sqrt{\sum_i \sigma_i^2} \approx 12\sigma$. This comparison demonstrates further the *huge* gain in signal and information obtained by adopting the tomographic approach.

We conclude this section comparing the CCFs of 2MPZ WI×SC and SDSS in the range $z \in [0.12, 0.4]$. In fact, given the fast-decreasing number of 2MPZ galaxies for $z > 0.2$, the vast majority of galaxies in this bin are in the range $z \in [0.12, 0.2]$. The most relevant comparison is thus made with the WI×SC and SDSS correlation in the range $z \in [0.1, 0.2]$. This is shown in Figure 17 for the energy bin [1, 10] GeV. It can be seen that while the SDSS and WI×SC cross-correlations are similar to each other, with the SDSS one slightly larger, the 2MPZ one is quite different, being higher by a factor of ∼3. This clearly suggests that the population of 2MPZ galaxies in $z \in [0.12, 0.4]$ is quite different from the one present in SDSS and WI×SC in the same redshift range. The high normalization of the cross-correlation further suggests that high-redshift 2MPZ sources have a very large bias, consistent with the one obtained from the 2MPZ autocorrelation analyses (Francis & Peacock 2010; Steward 2014).

6.6. Redshift Dependence of the Cross-correlation Signals

Finally, we combine the information from all catalogs to investigate the redshift dependence of the cross-correlation signal. To this purpose, we consider the sum $C_{1h} + A_{2h} \times C_{\ell=80}$ measured in the three wide energy bins in all of the catalogs and look for a dependence on z. We did not consider the 1- and 2-halo terms individually since the errors are too large for this analysis. The results are summarized in the three panels of Figure 18. All types of sources have been considered here, except the NVSS ones, for which we do not know the individual

redshifts. The data points represent effectively the correlation per unit redshift, and the plot can thus be seen as the distribution in redshift of the correlation.

The redshift distributions in the energy ranges 0.5–1 GeV and 1–10 GeV are quite similar. They both increase slowly from $z = 0$ to $z \sim 0.5$ and seem to drop at higher redshifts, although the large errors in the QSO data points do not allow us to draw a strong conclusion. At higher energy, the behavior of the distribution is different: the bulk of the correlation is generated at $z < 0.2$, while almost no correlation signal is detected at higher redshifts. Again, the errors in the QSO data points are too large to derive firm conclusions, but, in this case, the above picture is supported by the four high-z SDSS data points, which have smaller errors.

These plots contain precious information on the sources that contribute to the UGRB. However, to infer the latter, one needs to make some hypothesis on the bias of the different objects. We have assumed a linear bias, and this allowed us to absorb it in the normalization of the CCF. However, different types of objects may have different bias factors. If all objects considered had the same bias, then the plots would show the redshift distribution of the sources that generates the UGRB. However, we do know that different types of sources are characterized by different bias factors. For example, the 2MPZ data point at $z \sim 0.15$ in the energy range 1–10 GeV—a clear outlier—probably reflects the high bias of bright 2MPZ galaxies at high redshifts. QSOs are also highly biased. Their large bias factor ($b > 2$ at high redshift), thus, significantly enhances the cross-correlation signal.

A physically motivated cross-correlation model that includes hypothesis or independent constraints on the bias of the sources is therefore required to interpret the intriguing results shown in Figure 18. We postpone this task to a follow-up study.

7. Discussion and Conclusions

In this work, we have measured the angular cross-correlation between the cleaned P8 *Fermi*-LAT maps of the UGRB and different catalogs of extragalactic objects: NVSS, SDSS DR6 QSO, 2MPZ, *WISE* × SuperCOSMOS, and SDSS DR12 photometric. These data sets have been selected using the following criteria: (1) large sky coverage to sample as many ℓ modes as possible; (2) uniform preselection of objects across the relevant footprint; (3) wide span in redshift, from $z = 0$ up to $z \sim 5$, with a significant spatial overlap between the samples. The last requirement, also adopted by X15, has allowed those authors to perform a first coarse-grained, tomographic analysis of the cross-correlation signal, which turned out to be a powerful tool to investigate the nature of the UGRB. We took up from X15 and improved the original analyses in several aspects:

1. We used the Pass 8 *Fermi*-LAT γ-ray data. Thanks to the improved photon statistics, we were able to perform our cross-correlation study in several (up to eight) nonoverlapping energy bins.
2. Apart from NVSS, objects in the catalogs come with a redshift estimate, in the present analysis provided by *photometric* redshifts. Their error is much larger than of the spectroscopic ones but sufficiently small to enable us to slice up the catalogs into redshift bins, vastly improving the tomographic aspect of the analysis.
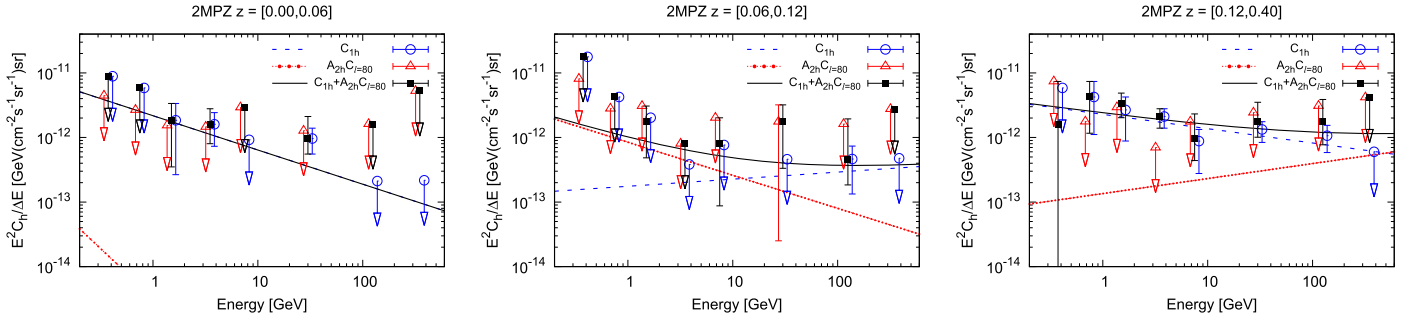
Figure 12. Same as Figure 8 but for the CAPS of 2MPZ galaxies measured in three redshift bins: $z \in [0, 0.06]$ (left), $z \in [0.06, 0.12]$ (middle), and $z \in [0.06, 0.4]$ (right).
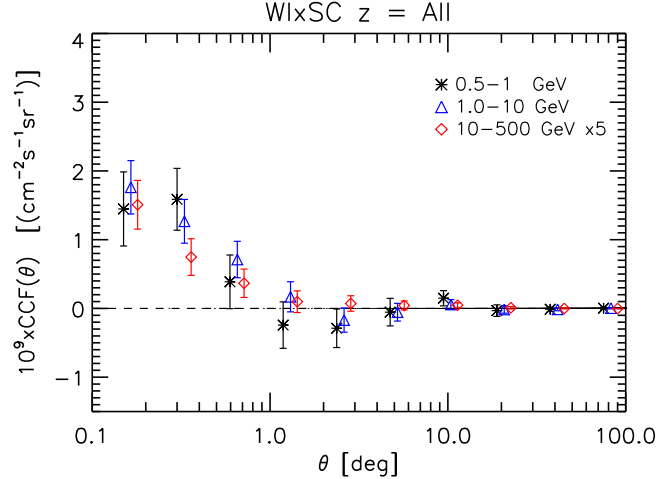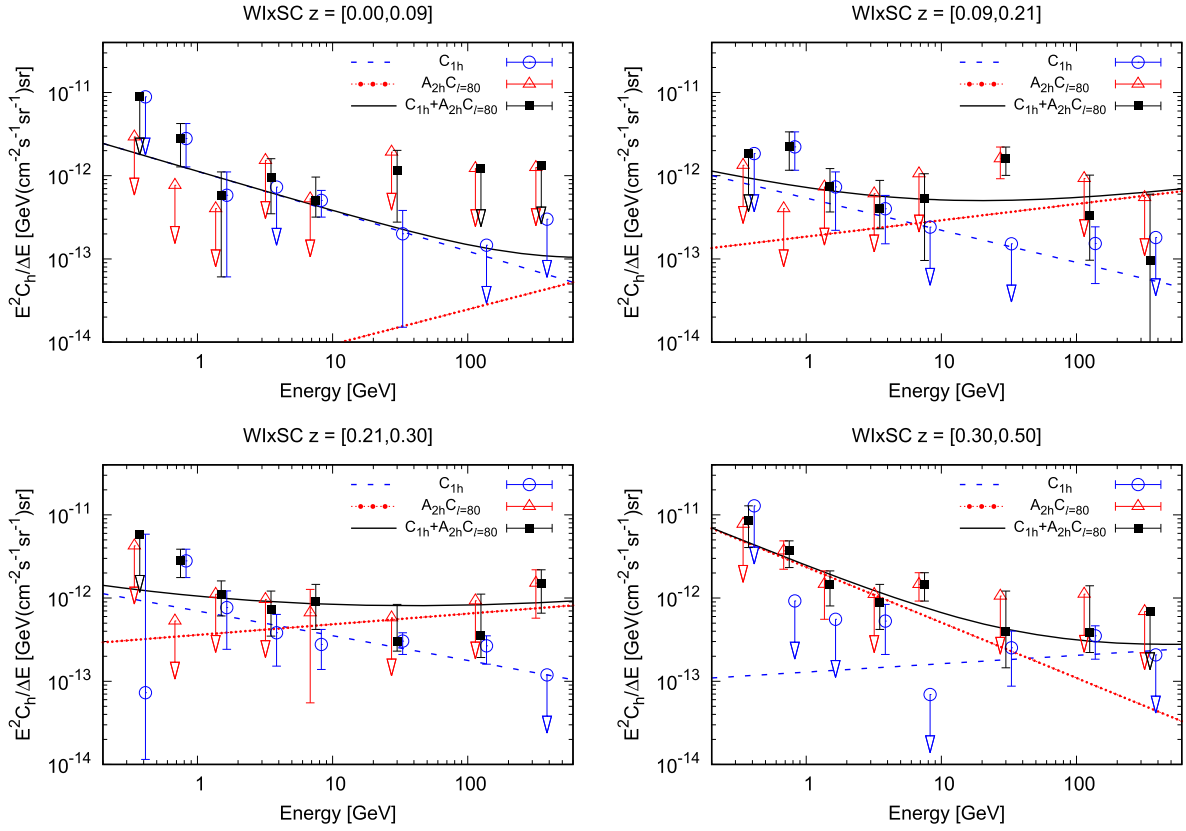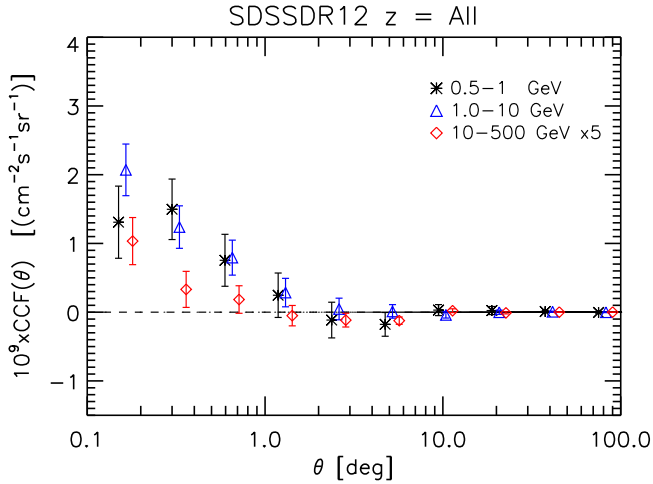

Figure 13. Same as the left panel of Figure 7 but for the cross-correlation of the full WI×SC sample with *Fermi*-LAT P8 data.

3. We fixed a normalization issue that has affected the amplitude of the correlations measured by X15.

Further, data files of our cross-correlation analysis both in configuration and harmonic space are publicly available at https://www-glast.stanford.edu/pub_data/.

The combination of good energy resolution and the availability of photometric redshifts allowed us to explore the energy and redshift dependence of the cross-correlation signal. In our analysis, we found that the UGRB is significantly correlated with the spatial distribution of all types of mass tracers that we have considered. The amplitude, angular scale, and energy band in which the correlation is detected vary with the type of objects and their redshift. A few general conclusions can be drawn:

1. The CCF analysis of a catalog not divided into redshift bins provides partial information on the nature of the γ-ray sources. In fact, it may also lead to biased results in those cases in which the cross-correlation signal is generated in different and well-localized redshift bins.

2. The fact that in various cases a significant variation of the signal as a function of energy and redshift is observed strongly suggests that the UGRB is produced by different types of sources, as indicated also by recent population studies of resolved γ-ray sources (Ajello et al. 2015; Fornasa & Sanchez-Conde 2015).

3. When considering the same z bin, different types of tracers produce different CCF signals. This is, for example, the case of the CCFs of 2MPZ, WI×SC, and SDSS DR12 in the range $0.1 \lesssim z \lesssim 0.2$ and for $E \in [1, 10]$ GeV. These dissimilarities reflect the differences in the relative bias between γ-ray sources and galaxies in the various catalogs, that is, the fact that different types of galaxies are more or less effective tracers of the unresolved γ-ray sources.

4. The CCF signal is rather compact in size. It rarely extends beyond $\theta = 1°$. In some cases it is even more compact ($\theta \lesssim 0°.4$ as in the NVSS case for $E > 10$ GeV). To analyze quantitatively the information encoded in the CCF as a function of energy and redshift, we have compared our measurements with the predictions of a simple model, inspired by the halo model, in which the cross-correlation signal is contributed by a compact 1-halo term and a more extended 2-halo term. Both the modeling and the analysis were performed in harmonic rather than configuration space to minimize error covariance. The use of this simple, yet physically motivated, general-purpose model, allows us to properly quantify the significance of the CCF signal, which, in several cases, can be quite large (i.e., $>5\sigma$, see Tables 2 and 4). The 1-halo term often dominates over the 2-halo one, hence justifying the compactness of the CCF. However, a 2-halo term is clearly detected in several energy and redshift ranges and, in some cases, is more prominent than the 1-halo one. This diversity provides further evidence in favor of the multisource hypothesis for the UGRB.

We postpone a detailed study of these results to a follow-up analysis in which the wealth of information produced in this work will be compared with more realistic UGRB models contributed by known (blazars, SFGs, misaligned AGNs) as well as hypothetical (annihilating or decaying DM particles) γ-ray sources. However, even our simple model can extract some additional information by exploring in more detail the energy dependence of the cross-correlation signal. Thanks to the exquisite photon statistics and energy resolution, we were able to compute the cross-correlation in eight energy bins and to compare the results with our model in which we allowed for an explicit energy dependence of the 1-halo and 2-halo terms. We modeled the energy dependence in three different ways: a single, a double, and a broken power law. We found the following:

Figure 14. Same as Figure 8 but for the CAPS of WI×SC galaxies measured in four redshift bins: $z \in [0.00, 0.09]$ (top left), $z \in [0.09, 0.21]$ (top right), $z \in [0.21, 0.30]$ (bottom left), $z \in [0.30, 0.50]$ (bottom right).

Figure 15. Same as the left panel of Figure 7 but for the cross-correlation of the full SDSS DR12 sample with *Fermi*-LAT P8 data.

1. The SPL, DPL, and BPL models typically provide similarly good fits. Nonetheless, various cases show some hint of preference for the DPL model, that is, a different slope for the 1-halo and 2-halo energy spectra.

2. More often than not, the energy spectrum of the 2-halo term is harder than that of the 1-halo term. However, some counterexamples are also seen. This further suggests the presence of different populations of γ-ray sources characterized by different spatial distributions and spectral properties.

3. An intriguing bump is seen at $E \sim 10$ GeV and $z \in [0.3, 0.5]$ in both SDSS DR12 and WI×SC. The bump is visible in the 2-halo term only. Although we did not attempt to quantify the significance of this feature, we note that an interpretation in the framework of a UGRB generated by conventional astrophysical sources would be rather challenging, while a bump in the energy spectrum in the 2-halo term would have a natural explanation in terms of DM annihilation.

4. Combining the information from all of the catalogs, we have been able to investigate the redshift distribution of the cross-correlation signal as a function of the redshift. We found that for energies below 10 GeV the signal increases with the redshift up to $z \sim 0.5$ and then decreases. Above 10 GeV, the correlation signal is mostly confined to low redshift ($z \lesssim 0.3$) with some additional contribution above $z \sim 1$. While these results support the hypothesis of multiple source populations contributing to the UGRB, drawing conclusions on the nature of these sources requires a physically motivated model of the UGRB. We postpone such analysis to a follow-up study.

In conclusion, we present a new way to characterize the UGRB by extracting accurate spectral and *redshift* information otherwise inaccessible when using γ-ray data alone. In the present study, we have only started to explore the implications of the wealth of new information made available by the
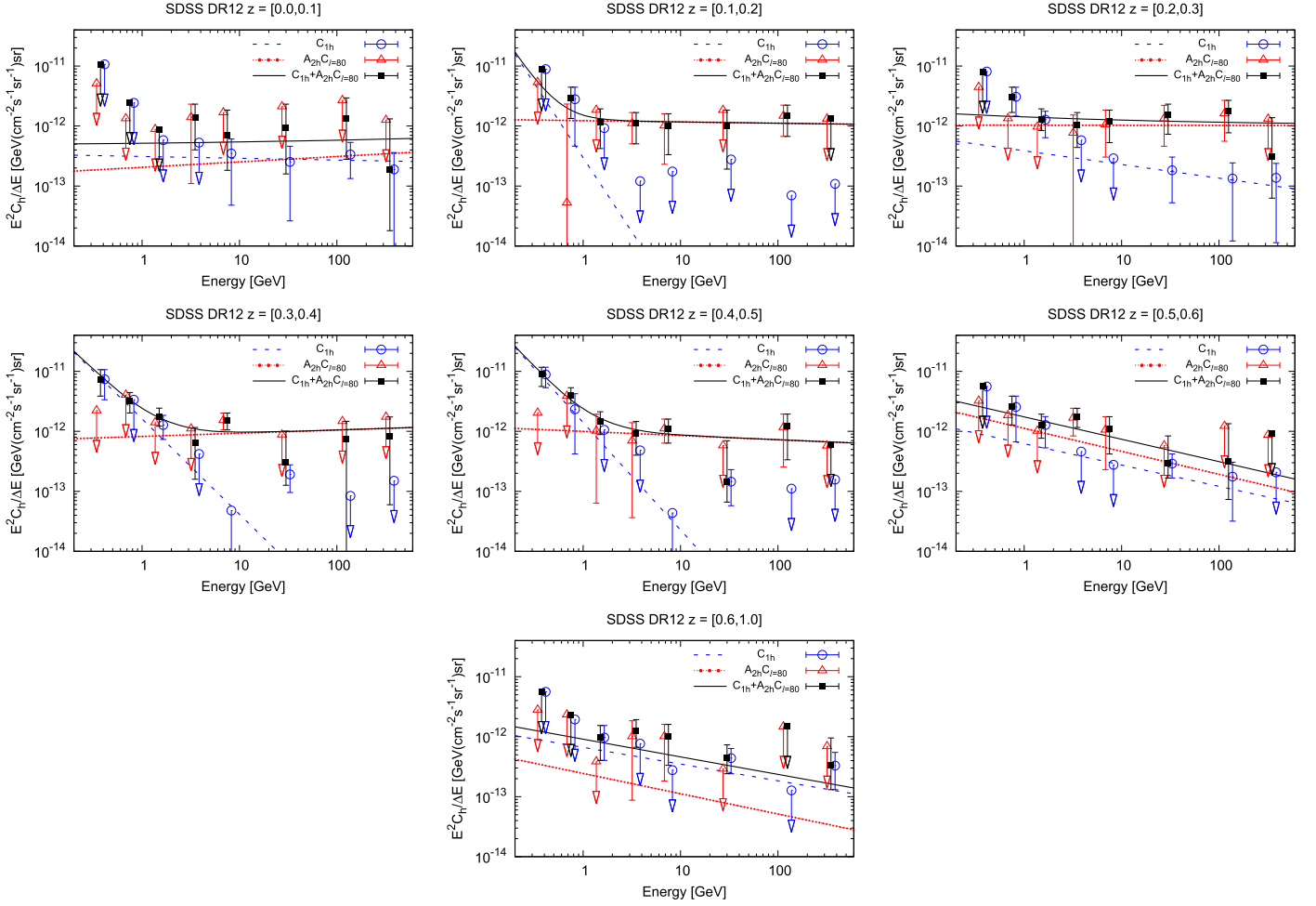
Figure 16. Same as Figure 8 but for the CAPS of SDSS DR12 galaxies measured in seven redshift bins: $z \in [0.0, 0.1]$, $z \in [0.1, 0.2]$, $z \in [0.2, 0.3]$, $z \in [0.3, 0.4]$, $z \in [0.4, 0.5]$, $z \in [0.5, 0.6]$, $z \in [0.6, 1.0]$.
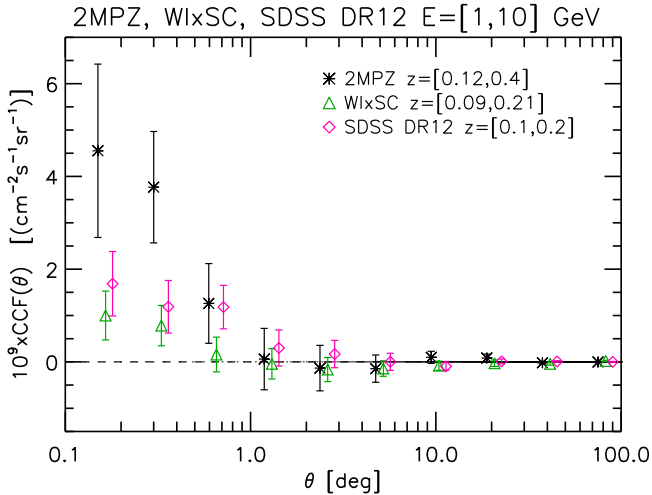
Figure 17. CCF of *Fermi*-LAT data in the energy range 1–10 GeV with 2MPZ galaxies for $z \in [0.12, 0.4]$, WI×SC galaxies for $z \in [0.09, 0.21]$, and SDSS DR12 galaxies for $z \in [0.1, 0.2]$. Note that, due to the decreasing redshift tail of 2MPZ, the range $z \in [0.12, 0.2]$ contains basically almost all of the galaxies of $z \in [0.12, 0.4]$.

tomography technique. In the near future, by exploiting these new data within the framework of well-motivated γ-ray population models, we shall set tighter constraints on the

nature of the UGRB sources, whether of astrophysical origin or not.

Figure 18. Dependence of the fitted Fermi-LAT γ-ray data–catalog cross-correlation signal, $C^{1h} + A^{2h}C^{2h}_{\ell=80}$, as a function of redshift, for three energy bins, as indicated in the plots.

Appendix A
Validation Tests

To validate the results presented in the main text, we have performed several tests described below. These have been
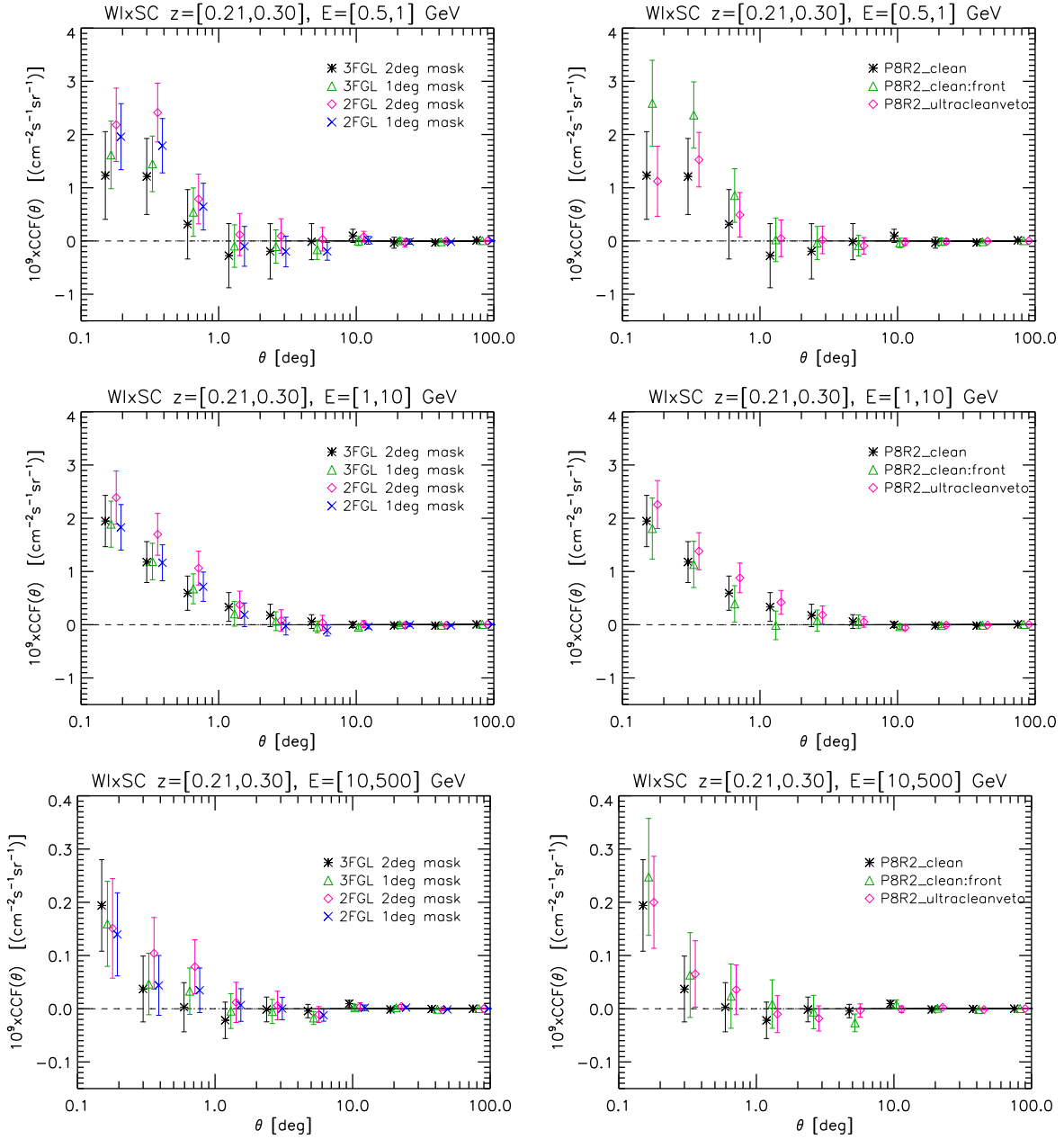
---

[15] http://www.star.bristol.ac.uk/~mbt/topcat/
[16] http://www.star.bristol.ac.uk/~mbt/stilts/
[17] http://healpix.sourceforge.net/

Figure 19. Angular CCF for WI×SC galaxies in the redshift bin $z \in [0.21, 0.30]$ for different γ-ray energy bins and different γ-ray point-source masks or γ-ray data selections, as indicated in the plot labels and described in the text. Error bars represent the square root of the diagonal elements of the covariance matrix.

performed using all subcatalogs considered in the cross-correlation analysis. Here we show the representative case of the WI×SC galaxies in the bin $z \in [0.21, 0.30]$. Very similar results have been found for all other subsamples analyzed.

Mask. The left column of Figure 19 illustrates the impact of changing the mask used to remove the γ-ray point sources. Our baseline is that of masking the brightest (in terms of the integral photon flux in the energy range [0.1, 100] GeV) 500 3FGL point sources with a disk of $2°$ radius, and the remaining ones with a $1°$ disk. We considered three more cases: (1) all 3FGL sources are masked with $1°$ disks, (2) all 2FGL sources are masked with $2°$ disks, and (3) all 2FGL sources are masked with $1°$ disks. It is clear from the plots that the impact of these different masks is negligible as all of the CCFs are consistent

with each other. These results deserve some further consideration. A dependence of the correlation on the mask is to be expected. For example, in Fornasa et al. (2016), it was shown that the γ-ray autocorrelation depends significantly on the catalog used to mask the point sources, with the anisotropy for the case of the 2FGL mask being a factor of ~ 4 larger than the case of the 3FGL mask. This implies that sources that are in the 3FGL catalog but not in the 2FGL one are responsible for the bulk of the anisotropy detected when using the 2FGL mask. A similar effect would be expected also for the cross-correlation, although, evidently, at a much smaller level. The fact that, from Figure 19, the cross-correlation for the 2FGL mask is consistent with the 3FGL mask case sets an upper limit on the magnitude of this effect that cannot exceed the random
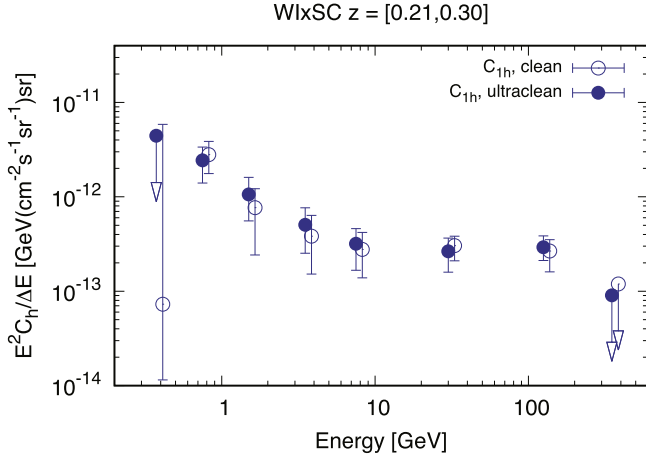
WIxSC z = [0.21,0.30]

Figure 20. The 1-halo term as a function of energy for the `P8R2_ULTRA-CLEANVETO_V6` and `P8R2_CLEAN_V6` cases.
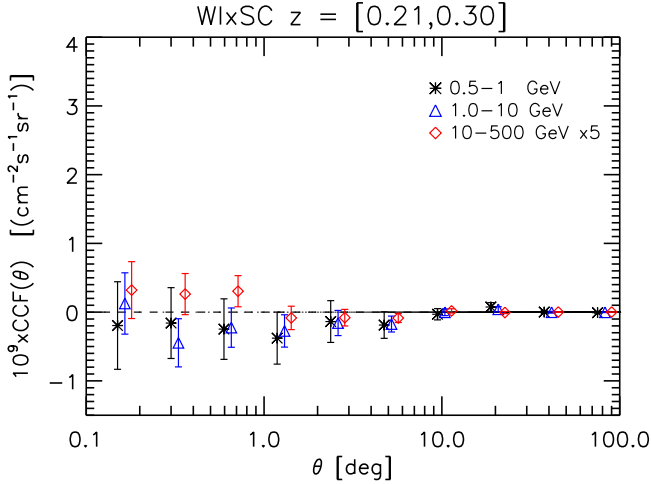
WIxSC z = [0.21,0.30]

Figure 21. Same as Figure 13 except that the angular coordinates of WI×SC galaxies have been transformed as $(l, b) \rightarrow (l, -b)$.

the different available classes. Increasing purity comes at the price of reducing the effective area by ~30% with respect to the `P8R2_CLEAN_V6` case. The tighter choice of a zenith angle cut of 90° instead of 100° removes more aggressively any residual contamination from the bright γ-ray Earth Limb. The right-hand panels of Figure 19 show the CCF that we measure when `P8R2_ULTRACLEANVETO_V6` is adopted. Figure 20, instead, compares the energy dependence of the 1-halo terms in the two cases. The results obtained using the two selection procedures are fully consistent with each other.

Data subsample. As a further test, we have considered only FRONT events. The FRONT data amount to about half of the total, with a better PSF, about ~50% more compact than the global average. The corresponding CCF, shown, again, in the right-hand panels of Figure 19, has a slightly larger amplitude in the energy bin $E \in [0.5, 1.0]$ GeV. This is not surprising. It reflects the convolution effect of a PSF that is more compact than the standard one. Once the signal is deconvolved from the PSF, like in the CAPS case, the correlation signal obtained using the `P8R2_CLEAN_V6:FRONT` data is fully consistent with the standard one.

No signal tests. Finally, Figure 21 is analogous to Figure 13 except for the fact that the Galactic latitude b of each object has been switched to $-b$. The same transformation has been applied to the angular coordinates of the pixels of the WI×SC mask. This transformation is expected to preserve the angular autocorrelation of WI×SC galaxies and remove the cross-correlation signal. The figure shows that this is indeed the case. No spurious cross-correlation is detected.

Appendix B
Additional Results

In this section, we show all of the results of the analyses that were not presented in the main text. This includes various sets of plots illustrating the CCFs of different catalogs, namely (1) three z shells extracted from the QSO DR6 sample (Figure 22), (2) four z shells extracted from the WI×SC sample (Figure 23), and (3) seven z shells extracted from the SDSS DR12 sample (Figure 24). A similar set of plots for the 2MPZ case has already been shown in the main text (Figure 11).

In addition we show two tables that summarize all of the results obtained in this work. Table 4 expands (and also includes) Table 2 and contains the results of the best fits to the CAPS of the different catalogs measured in all z bins and in three wide energy bins: $E \in [0.5, 1]$, $[1, 10]$, and $[10, 500]$ GeV.

Table 5 lists the best-fit parameters of the models that describe the energy dependence of the 1-halo and 2-halo terms that contribute to the CAPS. This table shows the results of all of the energy models: SPL, DPL, and BPL, whereas Table 3 in the main text only contains the DPL results.
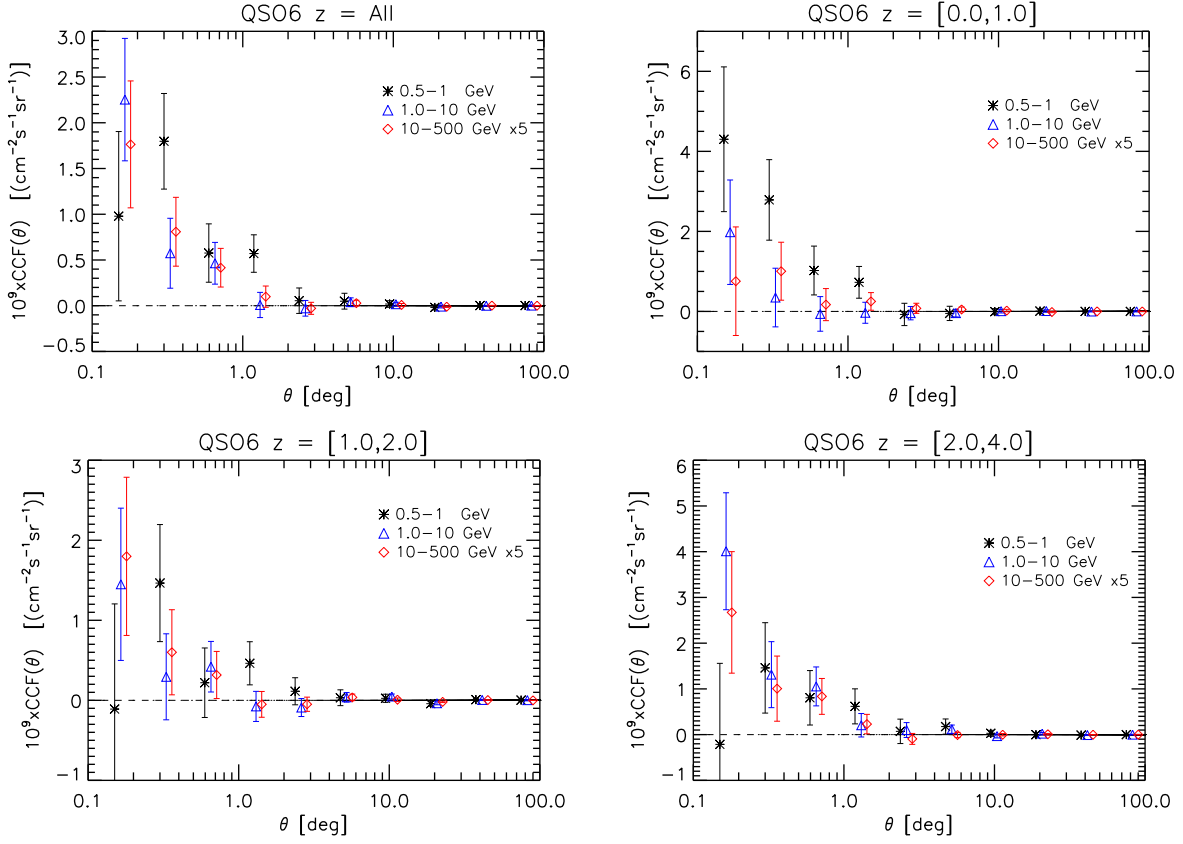
error; that is, it has to be smaller than 20%–30%. Indeed, we do detect this effect for the case of the NVSS catalog, for which the relative errors are the smallest, at the level of 5%–10%. In that case, the cross-correlation with 2FGL sources is ~20% larger than with the 3FGL ones.

Data class. The effect of changing the data selection procedure is illustrated in the right-hand panels of Figure 19. The default procedure is the `P8R2_CLEAN_V6` selection with a zenith angle cut of 100°. In the figure, we compare the standard CCF with the one obtained when γ-ray data are selected using the `P8R2_ULTRACLEANVETO_V6` with a zenith angle cut of 90°. This alternative selection has the lowest cosmic-ray contamination of the γ-ray sample among

Figure 22. Angular CCF for DR6 QSOs in different redshift and energy bins. The top left panel is for $z = $ All, top right for $z \in [0.0, 1.0]$, bottom left for $z \in [1.0, 2.0]$, and bottom right for $z \in [2.0, 4.0]$. Energy bins are $E \in [0.5, 1]$ GeV, $[1, 10]$ GeV, and $[10, 500]$ GeV.
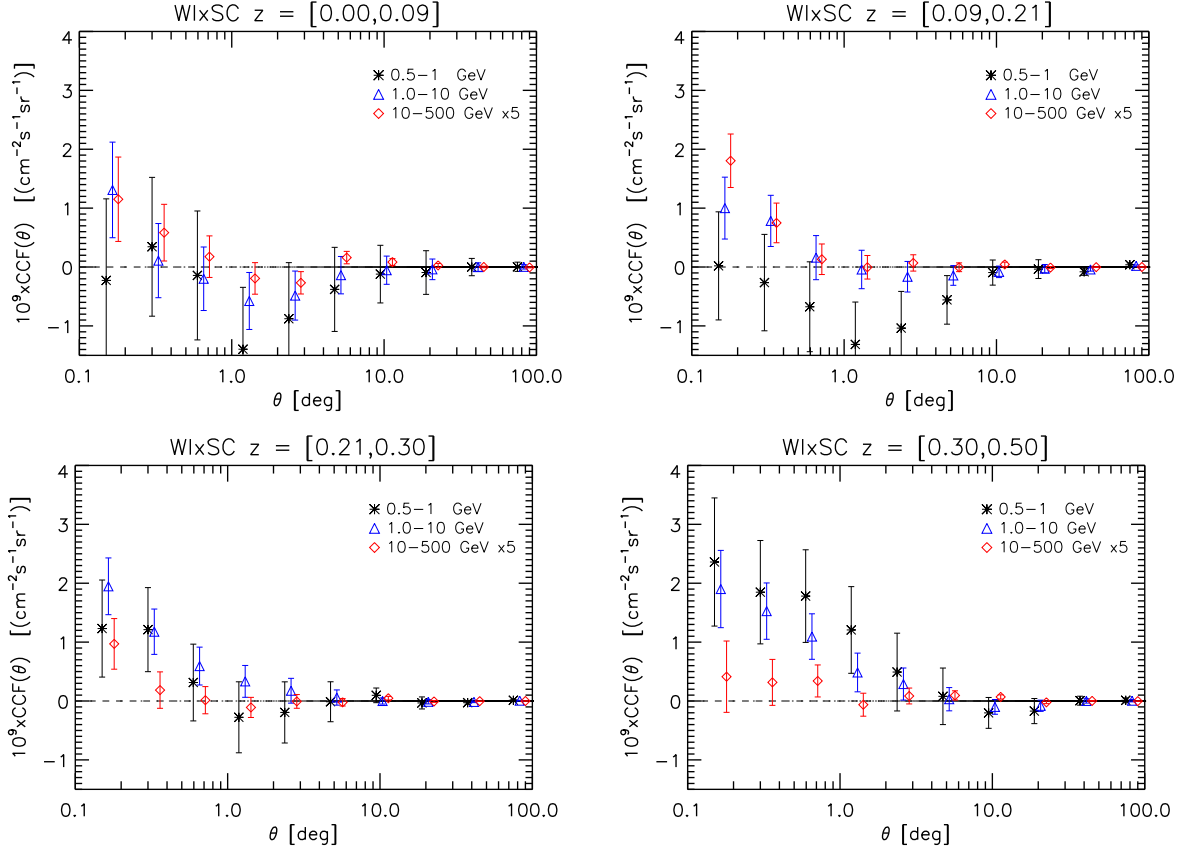

Figure 23. Angular CCF for WI×SC galaxies in different redshift and energy bins. The top left panel is for $z \in [0.0, 0.09]$, the top right panel is for $z \in [0.09, 0.21]$, the bottom left panel is for $z \in [0.21, 0.30]$, and the bottom right panel is for $z \in [0.30, 0.50]$. Energy bins are for $E \in [0.5, 1]$ GeV, $[1, 10]$ GeV, and $[10, 500]$ GeV.
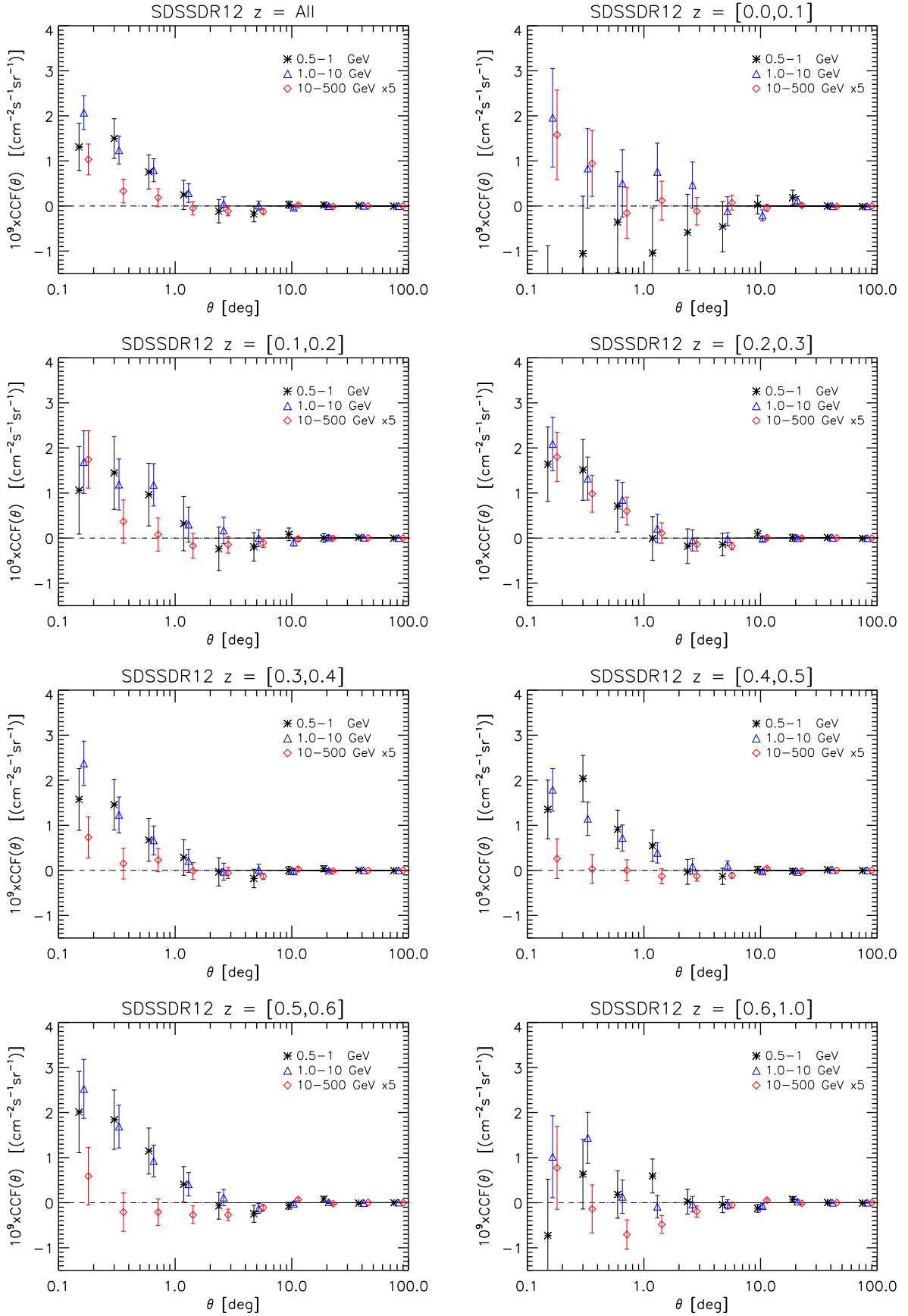
Figure 24. Angular CCF for SDSS DR12 galaxies in different redshift and energy bins. The top row is for $z =$ All and $z \in [0.0, 0.1]$, second row $z \in [0.1, 0.2]$ and $z \in [0.2, 0.3]$, third row $z \in [0.3, 0.4]$ and $z \in [0.4, 0.5]$, fourth row $z \in [0.5, 0.6]$ and $z \in [0.6, 1.0]$. Energy bins are $E \in [0.5, 1]$ GeV, $[1, 10]$ GeV, and $[10, 500]$ GeV.

ORCID iDs

Maciej Bilicki ⊙ https://orcid.org/0000-0002-3910-5809
Jun-Qing Xia ⊙ https://orcid.org/0000-0003-4621-754X
Enzo Branchini ⊙ https://orcid.org/0000-0002-0808-6908

References

Abdalla, F. B., Banerji, M., Lahav, O., & Rashkov, V. 2011, MNRAS, 417, 1891
Acero, F., Ackermann, M., Ajello, M., et al. 2015, ApJS, 218, 23
Acero, F., Ackermann, M., Ajello, M., et al. 2016, ApJS, 223, 26
Ackermann, M., Ajello, M., Allafort, A., et al. 2012a, ApJ, 755, 164
Ackermann, M., Ajello, M., Atwood, W. B., et al. 2012b, ApJ, 750, 3
Ackermann, M., Johannesson, G., Digel, S., et al. 2009, in AIP Conf. Proc. 1085, 4th Int. Meeting on High Energy Gamma-Ray Astronomy, ed. F. A. Aharonian, W. Hofmann, & F. Rieger (Melville, NY: AIP), 763
Ackermann, M., Ajello, M., Allafort, A., et al. 2011, ApJ, 741, 30
Ackermann, M., Ajello, M., Albert, A., et al. 2012c, PhRvD, D85, 083007
Ackermann, M., Ajello, M., Albert, A., et al. 2015, ApJ, 799, 86
Ackermann, M., Ajello, M., Albert, A., et al. 2016, PhRvL, 116, 151105
Aihara, H., Allende Prieto, C., An, D., et al. 2011, ApJS, 193, 29
Ajello, M., Gasparrini, D., Sánchez-Conde, M., et al. 2015, ApJL, 800, L27
Ajello, M., Romani, R. W., Gasparrini, D., et al. 2014, ApJ, 780, 73
Ajello, M., Shaw, M. S., Romani, R. W., et al. 2012, ApJ, 751, 108
Alam, S., Albareti, F. D., Allende Prieto, C., et al. 2015, ApJS, 219, 12
Alonso, D., Salvador, A. I., Sánchez, F. J., et al. 2015, MNRAS, 449, 670
Ando, S. 2009, PhRvD, 80, 023520
Ando, S. 2014, JCAP, 1410, 061
Ando, S., Benoit-Lvy, A., & Komatsu, E. 2014, PhRvD, D90, 023514
Ando, S., Benoit-Lvy, A., & Komatsu, E. 2017, arXiv:1706.05422
Ando, S., Fornasa, M., Fornengo, N., Regis, M., & Zechlin, H.-S. 2017, arXiv:1701.06988
Ando, S., & Komatsu, E. 2006, PhRvD, 73, 023521
Ando, S., & Komatsu, E. 2013, PhRvD, 87, 123539
Atwood, W., Albert, A., Baldini, L., et al. 2013, arXiv:1303.3514
Atwood, W. B., Abdo, A. A., Ackermann, M., et al. 2009, ApJ, 697, 1071
Beck, R., Dobos, L., Budavári, T., Szalay, A. S., & Csabai, I. 2016, MNRAS, 460, 1371
Bilicki, M., Jarrett, T. H., Peacock, J. A., Cluver, M. E., & Steward, L. 2014, ApJS, 210, 9
Bilicki, M., Peacock, J. A., Jarrett, T. H., et al. 2016, ApJS, 225, 5
Branchini, E., Camera, S., Cuoco, A., et al. 2017, ApJS, 228, 8
Brookes, M. H., Best, P. N., Peacock, J. A., Röttgering, H. J. A., & Dunlop, J. S. 2008, MNRAS, 385, 1297
Camera, S., Fornasa, M., Fornengo, N., & Regis, M. 2015, JCAP, 1506, 029
Casandjian, J., Grenier, I. & For The Fermi Large Area Telescope Collaboration 2009, arXiv:0912.3478
Challinor, A., & Chon, G. 2005, MNRAS, 360, 509
Chon, G., Challinor, A., Prunet, S., Hivon, E., & Szapudi, I. 2004, MNRAS, 350, 914
Condon, J. J., Cotton, W. D., Greisen, E. W., et al. 1998, AJ, 115, 1693
Cooray, A., & Sheth, R. 2002, PhR, 372, 1
Cuoco, A., Komatsu, E., & Siegal-Gaskins, J. M. 2012, PhRvD, 86, 063004
Cuoco, A., Xia, J.-Q., Regis, M., et al. 2015, ApJS, 221, 29
de Zotti, G., Massardi, M., Negrello, M., & Wall, J. 2010, A&ARv, 18, 1
Di Mauro, M., Calore, F., Donato, F., Ajello, M., & Latronico, L. 2014a, ApJ, 780, 161

Di Mauro, M., Cuoco, A., Donato, F., & Siegal-Gaskins, J. M. 2014b, JCAP, 1411, 021
Di Mauro, M., Donato, F., Lamanna, G., Sanchez, D. A., & Serpico, P. D. 2014c, ApJ, 786, 129
Dodelson, S., Belikov, A. V., Hooper, D., & Serpico, P. 2009, PhRvD, 80, 083504
Efstathiou, G. 2004a, MNRAS, 348, 885
Efstathiou, G. 2004b, MNRAS, 349, 603
Feng, C., Cooray, A., & Keating, B. 2017, ApJ, 836, 127
Feyereisen, M. R., Ando, S., & Lee, S. K. 2015, JCAP, 1509, 027
Fornasa, M., Cuoco, A., Zavala, J., et al. 2016, PhRvD, 94, 123005
Fornasa, M., & Sanchez-Conde, M. A. 2015, PhR, 598, 1
Fornasa, M., Zavala, J., Sanchez-Conde, M. A., et al. 2013, MNRAS, 429, 1529
Fornengo, N., Perotto, L., Regis, M., & Camera, S. 2015, ApJL, 802, L1
Fornengo, N., & Regis, M. 2014, FrP, 2, 6
Francis, C. L., & Peacock, J. A. 2010, MNRAS, 406, 2
Górski, K. M., Hivon, E., Banday, A. J., et al. 2005, ApJ, 622, 759
Harding, J. P., & Abazajian, K. N. 2012, JCAP, 1211, 026
Inoue, Y. 2011, ApJ, 733, 66
Jarrett, T. 2004, PASA, 21, 396
Jarrett, T. H., Chester, T., Cutri, R., et al. 2000, AJ, 119, 2498
Komatsu, E., & Seljak, U. 2002, MNRAS, 336, 1256
Landy, S. D., & Szalay, A. S. 1993, ApJ, 412, 64
Lewis, A., Challinor, A., & Lasenby, A. 2000, ApJ, 538, 473
Lisanti, M., Mishra-Sharma, S., Necib, L., & Safdi, B. R. 2016, ApJ, 832, 117
Liske, J., Baldry, I. K., Driver, S. P., et al. 2015, MNRAS, 452, 2087
Malyshev, D., & Hogg, D. W. 2011, ApJ, 738, 181
Peacock, J. A., Hambly, N. C., Bilicki, M., et al. 2016, MNRAS, 462, 2085
Planck Collaboration, Ade, P. A. R., Aghanim, N., et al. 2014, A&A, 571, A15
Planck Collaboration, Ade, P. A. R., Aghanim, N., et al. 2016, A&A, 594, A13
Regis, M., Xia, J.-Q., Cuoco, A., et al. 2015, PhRvL, 114, 241301
Richards, G. T., Myers, A. D., Gray, A. G., et al. 2009, ApJS, 180, 67
Shirasaki, M., Horiuchi, S., & Yoshida, N. 2014, PhRvD, 90, 063502
Shirasaki, M., Macias, O., Horiuchi, S., Shirai, S., & Yoshida, N. 2016, PhRvD, 94, 063522
Smith, R. E., Peacock, J. A., Jenkins, A., et al. 2003, MNRAS, 341, 1311
Steward, L. 2014, Master's thesis, Univ. Cape Town
Su, M., Slatyer, T. R., & Finkbeiner, D. P. 2010, ApJ, 724, 1044
Szapudi, I., Prunet, S., & Colombi, S. 2001, ApJL, 561, L11
Takahashi, R., Sato, M., Nishimichi, T., Taruya, A., & Oguri, M. 2012, ApJ, 761, 152
Taylor, M. B. 2005, in ASP Conf. Ser. 347, Astronomical Data Analysis Software and Systems XIV, ed. P. Shopbell, M. Britton, & R. Ebert (San Francisco, CA: ASP), 29
Taylor, M. B. 2006, in ASP Conf. Ser. 351, Astronomical Data Analysis Software and Systems XV, ed. C. Gabriel et al. (San Francisco, CA: ASP), 666
Tröster, T., Camera, S., Fornasa, M., et al. 2017, MNRAS, 467, 2706
Wright, E. L., Eisenhardt, P. R. M., Mainzer, A. K., et al. 2010, AJ, 140, 1868
Xia, J., Viel, M., Baccigalupi, C., & Matarrese, S. 2009, JCAP, 9, 3
Xia, J.-Q., Cuoco, A., Branchini, E., Fornasa, M., & Viel, M. 2011, MNRAS, 416, 2247
Xia, J.-Q., Cuoco, A., Branchini, E., & Viel, M. 2015, ApJS, 217, 15
Zechlin, H.-S., Cuoco, A., Donato, F., Fornengo, N., & Regis, M. 2016a, ApJL, 826, L31
Zechlin, H.-S., Cuoco, A., Donato, F., Fornengo, N., & Vittino, A. 2016b, ApJS, 225, 18